ANALYSIS OF HEAT TRANSFER IN SUBCOOLED METAL POWDER SUBJECTED TO PULSED LASER HEATING

A Thesis
presented to the
Faculty of the Graduate School
University of Missouri – Columbia

In Partial Fulfillment
of the Requirement for the Degree

Master of Science

---

by
CHAD KONRAD

Dr. Yuwen Zhang, Thesis Supervisor

JULY 2005

The undersigned have examined the thesis entitled

ANALYSIS OF HEAT TRANSFER IN SUBCOOLED METAL POWDER SUBJECTED TO PULSED LASER HEATING

Presented by Chad Konrad

A candidate for the degree of Master of Science

And hereby certify that in their opinion it is worthy of acceptance

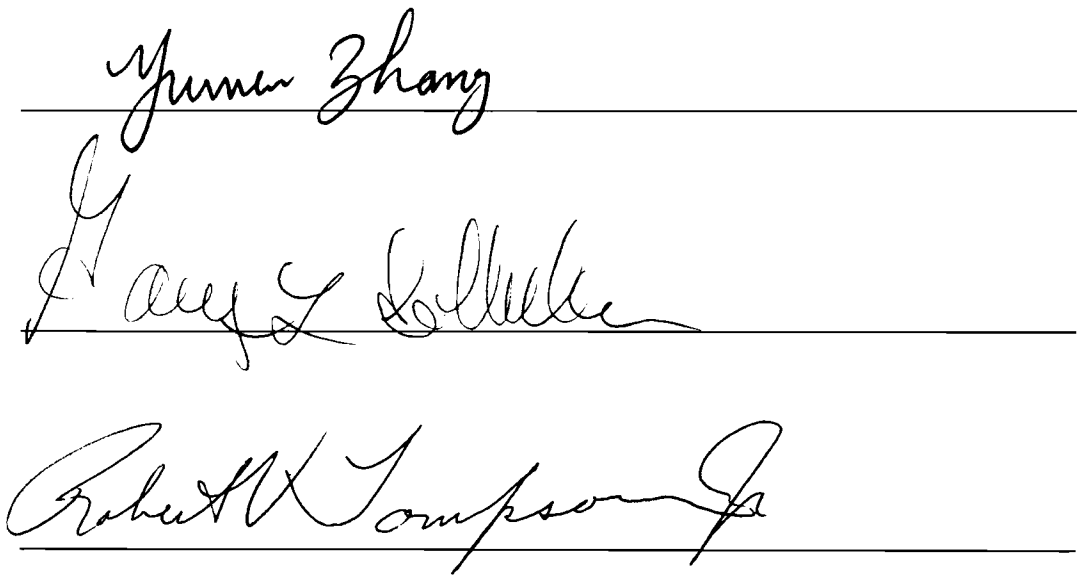

ACKNOWLEDGEMENTS

I would like to thank Dr. Zhang for providing much needed guidance and assistance on this project.

Special thanks to Mom and Dad.

Support for this work provided by the Office of Naval Research (ONR) under grant number N00014-04-1-0303 is gratefully acknowledged.

TABLE OF CONTENTS

LIST OF FIGURES

ANALYSIS OF HEAT TRANSFER IN SUBCOOLED METAL POWDER SUBJECTED TO PULSED LASER HEATING

Chad Konrad

Dr. Yuwen Zhang, Thesis Supervisor

ABSTRACT

The interaction of metal powder and pulsed laser heat flux is investigated on two levels, the powder bed level and the particle level. The locations of the thermal penetration depth and the liquid-solid interface are obtained using the integral approximate method. Melting and resolidification of a subcooled, two-component metal powder bed subjected to temporal Gaussian heat flux is investigated analytically. An increase in heat source intensity or powder bed porosity will result in an increase of the melt pool depth, melt pool temperature, and the overall processing time. The melt pool becomes shallower with increasing subcooling. Heat conduction in a single subcooled metal powder particle subjected to nanosecond pulsed laser heating is also investigated analytically. A change in the repetition rate of the laser or an increase in maximum heat flux will result in a larger temperature rise on the surface of the particle, as well as a higher thermalized particle temperature after the laser pulse is finished. Although a discrepancy exists where peak surface temperatures are concerned, the thermalized temperatures of different-sized spheres are all the same. The time at which the particle is fully penetrated is only affected by a change in thermal diffusivity, laser pulse width, or particle radius. The physical model and results of this investigation pave the way for further modeling of Selective Laser Sintering (SLS) processes with a pulsed laser.

NOMENCLATURE

h_{sl} latent heat of fusion [$J \cdot kg^{-1}$]

k thermal conductivity [$W \cdot m^{-1} \cdot {}^{\circ} C^{-1}$]

K dimensionless thermal conductivity

$q"$ heat flux [$W \cdot m^{-2}$]

s solid-liquid interface location [m]

s_0 location of liquid surface [m]

S dimensionless solid-liquid interface location

S_0 dimensionless location of liquid surface

Sc subcooling parameter

Ste Stefan number

t time [s]

t_p half width of the laser beam pulse at 1/e [s]

T temperature [${}^{\circ} C$]

w velocity of liquid phase [$m \cdot s^{-1}$]

W dimensionless velocity of the liquid phase

x coordinate [m]

z coordinate [m]

Z dimensionless coordinate

Greek Symbols

α thermal diffusivity [$m^2 \cdot s^{-1}$]

$\bar{\alpha}$ dimensionless thermal diffusivity

δ thickness of thermal layer [m]

Δ dimensionless thickness of thermal layer

ε volume fraction of gas(es) (porosity for unsintered powder)

θ dimensionless temperature (Chapter 2) or excess temperature [$^{\circ}C$] (Chapter 3)

ρ density [$kg \cdot m^{-3}$]

τ dimensionless time

τ_p half width of the laser beam pulse at $\frac{1}{2} q_0^{"}$ [s]

ϕ volume fraction of the low melting point powder in the powder mixture

Subscripts

0 beginning (when preheating begins)

final final (when solidification ends)

g gas(es)

H high melting point metal

i initial

ℓ liquid phase (mixture of low melting point metal liquid and high melting point powder solid)

L low melting point powder

m melting point (when melting begins)

p fully densified resolidified part

r resolidified part

s unsintered solid (mixture of two solid powders)

sol solidification (when solidification begins)

Chapter 1. Introduction

Selective Laser Sintering (SLS) is an emerging technology that can build structurally-sound parts from powdered material via layer-by-layer sintering (for amorphous powder, such as polycarbonate) or melting (for crystalline powder, such as metal) induced by a directed laser beam. Fabrication of metal parts is a very challenging task since the temperature required to bind the metal powder particles is much higher than that needed to bind the amorphous powder particles. SLS is a very useful rapid manufacturing method because it allows for the manufacture of complex parts often unobtainable by more common manufacturing processes [1, 2]. During the SLS process the surface of a powder bed is scanned with a laser heat source to melt the powder and as the beam moves away the liquid resolidifies into a solid. Another layer of powder is then pushed over the newly solidified surface and the process is repeated, thus building a solid object layer by layer.

Recent advances in metallic SLS have improved the technology, but it still remains limited in terms of material versatility, quality, and precision [3]. The behaviors of the powders used in SLS processes are quite different depending on the material, the shape and size of powder particles and so on, and it is necessary to use a trial and error method to find suitable materials for an SLS process [4]. It is for these reasons that a sound theoretical SLS model must be developed so that the results of SLS techniques and the quality of the parts can be predicted accurately.

There are other obstacles that must also be overcome before SLS can be used for mass production of final, high quality parts that exhibit good surface finish and desirable

mechanical properties. One such obstacle is the balling phenomenon [5], in which melted powder grains stick to each other via surface tension forces, thereby forming a series of spheres with diameters approximately equal to the diameter of the laser beam. The balling phenomenon is well documented, an extensive study of which can be found in Tolochko et al. [5].

There are several ways the balling phenomenon can be combated, one of which is to use a powder bed consisting of two different types of metal powder, one with a significantly higher melting point than the other as suggested by Bunnell [6] and Manzur et al. [7]. If such a mixture is used the higher melting point powder will not melt, breaking up the surface tension forces and forcing out the interstitial gasses as desired. An analytical one-dimensional analysis of this phenomenon can be found in Konrad et al. [8], in which the effects of the porosities, Stefan number, and subcooling on the surface temperature and solid-liquid interface were investigated. Zhang and Faghri [9] analytically solved a one-dimensional melting problem in a semi-infinite two-component metal powder bed subjected to *constant* heat flux. The effects of the porosity of the loose powder and liquid, initial subcooling parameter, and dimensionless thermal conductivity of the interstitial gas were investigated. Chen and Zhang [10] obtained the analytical solution of melting in a two-component powder layer with finite thickness subject to *constant* heat flux.

Another way to minimize the balling effect is to use a pulsed laser to decrease the life span of the melt pool and thus help avoid the balling effect [11]. In a traditional SLS process a high-power CO_2 laser scans the surface of the metal powder bed, homogeneously heating the grains. If a low-power, short-pulse laser is used, however,

the high intensity pulses will heat the outer surface of the powder grain to a very high temperature yet leave the interior of the grain at the ambient temperature. If enough pulses are used, the outer surfaces of the powder grains will melt, join together and, within several microseconds, resolidify as the cool interior portion of the powder grain acts as a heat sink to draw in the latent heat of the outer liquid layer. Using this sintering mechanism, powder grains will be joined at a much lower average temperature using moderate laser power, typically less than 10W, as well as minimizing balling effects and introducing less residual stress in the workpiece [12]. When a pulsed Nd:YAG laser is used this process will yield higher lateral precision than the CO_2 process due to its smaller wavelength. In addition, the degree of partial melting and ultimately, the local porosity in the final product can be easily controlled.

A recent thermal model proposed by Fischer et al. [13] proposes modeling a pulsed SLS process by focusing on the melting and resolidification of a single grain of the powder bed in order to understand the process on a more fundamental level. The paper suggests two laser processing scenarios, the first of which consists of a low repetition rate and a high single pulse energy. These parameters result in the melting of a narrow skin layer on the surface of the particle with only one pulse, however, the strong recoil effect from such a high power pulse may result in blowing the powder away before any consolidation can take place. The other processing scenario calls for a high repetition rate with a low energy single pulse. In this case it takes a superposition of many pulses to raise the grain to its melting temperature, at which point sintering occurs. The time between pulses is long enough that thermalization can occur in the powder particle, leading to an average temperature that is higher than the previous initial temperature.

The fundamentals of melting and solidification have been investigated extensively [14,15], however, laser-induced melting of metal powder in SLS processes differs from conventional melting because the subcooled powder can consist of as much as 40-60% gas. During melting it is necessary for the liquid phase to collect and drive the interstitial gasses out of the powder bed, effectively "shrinking" the volume of the powder bed. It is because of this shrinkage phenomenon that the powder bed experiences a significant density change during the melting process, resulting in motion of the surface of the powder bed during the SLS process.

Although early research in SLS processes was conducted exclusively with Continuous Wave (CW) lasers, pulsed lasers with pulse widths ranging from milliseconds (Su et al. [16] and Abe et al. [4]) to nanoseconds (Morgan et al. [11] and Fischer et al. [3,12]) have also recently been used to sinter metal powders. Su et al. [16] investigated fully dense laser sintering of tool steel powder using a Nd:YAG laser with pulse widths between 0.5 and 20 ms and average power up to 550W. Abe et al. [4] studied SLS of titanium powders using a YAG laser with pulse widths from 1 to 5 ms and an average power of 50W. The average power levels of the millisecond lasers used by Su et al. [16] and Abe et al. [4] are comparable to that of a CW laser because the conduction heat loss into the unsintered region for a millisecond laser is similar to that of a CW laser.

The results of SLS experiments performed by Morgan et al. [11] on gas atomized 316L stainless steel using a nanosecond Nd:YAG laser showed that the vaporization recoil force overcame the surface tension forces acting on the melt, therefore improving the cohesion of the powder particles when compared to the CW SLS process. When a nanosecond laser is used to sinter metal powder the papers by Fischer et al. [3,13] suggest

that only a thin surface layer of the powder particle is melted and the core of the particle remains at its initial temperature, as described above. The temperature in this thin skin of liquid on the surface of the particle was estimated by a one-dimensional conduction model of a single spherical particle surrounded by a continuum that represents neighboring particles. Fischer et al. [3,12] performed SLS experiments on titanium powder with a nanosecond Nd:YAG laser operated at a pulse width of 150 ns and repetition rate between 1 and 30 kHz.

In order to discover the advantages of utilizing a pulsed laser in a SLS process, melting and resolidification of a two-component powder bed will be modeled. The effects of a change in heat source intensity, powder bed porosity, and subcooling parameter will be investigated. In addition to the powder bed level analysis, a particle level analysis will be conducted by examining heat conduction in a single spherical grain of metal powder. The effects of a change in laser pulse width, heat flux at the surface, thermal diffusivity, and particle radius on the simulation will also be investigated. This paper represents a fundamental study of the SLS process upon which more comprehensive models may be based on in the future.

Chapter 2. Melting and resolidification of a two-component powder bed

Melting and resolidification of a bed of powder particles subjected to temporal Gaussian heat flux from a laser beam will be modeled in this chapter. The diameter of the metal powder particles is much smaller than the diameter of the laser beam, which is in turn much smaller than the final desired part.

2.1 Physical model

The physical model of melting and resolidification is shown in Fig. 2.1.

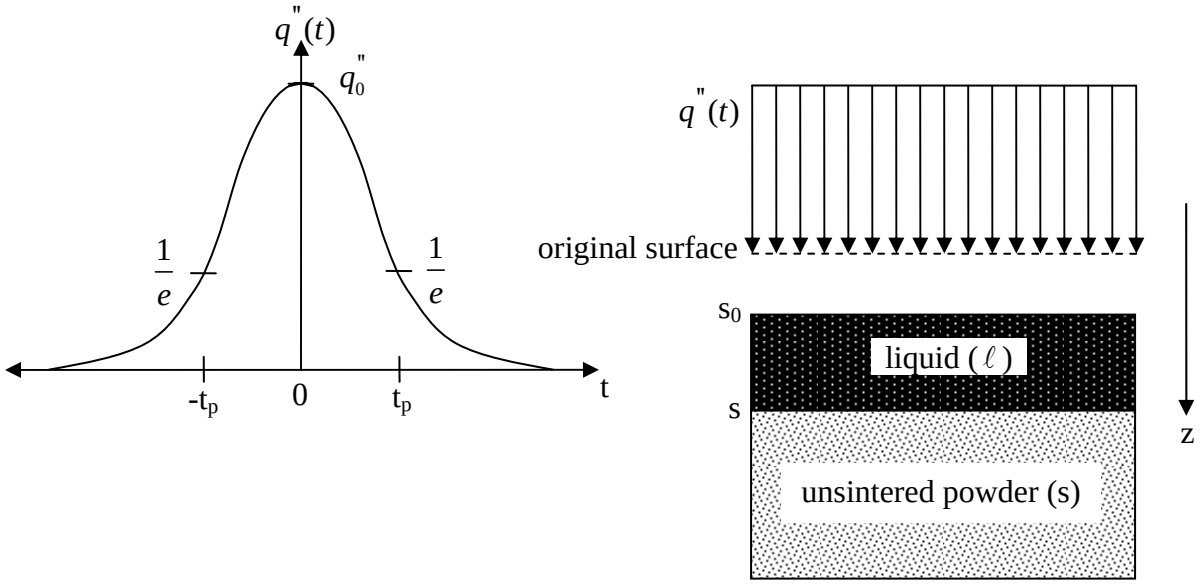

Figure 2.1 The physical model.

The initial temperature of the powder bed of infinite thickness, which contains two metal powders with significantly different melting points, is well below the melting temperature of the low melting point metal powder component. The origin of time is

chosen to be the time at which the heat flux is at its maximum, thus the time-dependent heat flux is

$$q''(t) = q_0'' e^{-\frac{t^2}{t_p^2}} \tag{1}$$

Although the *origin* of time, $t = 0$, is chosen to be when the heat flux is at its maximum, the time at which the simulation begins will be $t = -\infty$ so that the entire pulse energy is used.

The laser-powder bed interaction can be divided into three stages: (1) preheating, (2) melting with shrinkage, and (3) resolidification. During the preheating period the powder bed must absorb a significant amount of heat to bring the powder bed surface temperature up to the melting temperature of the low melting point powder, T_m. The duration of the preheating stage is defined as the time it will take for the surface temperature to reach T_m. The melting stage begins after the surface temperature of the powder bed has reached the melting temperature of the low-melting point powder. During this period the powder melts rapidly and consolidates into a liquid pool. This consolidation results from the fact that the liquid cannot maintain the relatively high initial porosity of the solid powder bed and therefore the interstitial gasses are driven out of the liquid pool. This consolidation of the powder bed results in a significant density change, and thus liquid surface motion. The resulting liquid pool is not fully dense, in other words some interstitial gas is still trapped within the liquid phase, because the liquid lifetime is very short. It should be restated that the metal with the higher melting point will not melt during the entire process. The surface heat flux will reach its maximum at time $t = 0$, after which the heat flux will begin to decrease. This will result in a cooling of the melt pool and eventually

resolidification into a solid layer. When the pool has completely resolidified, the process is over and the resolidified part will begin to cool to the ambient temperature.

This chapter presents analysis of a one dimensional model of the phase change undergone by the first layer of the SLS process on a cold powder bed. The true SLS process is, of course, a three dimensional, multiple-layer process in which layer after layer of powder is added to the surface of the bed. A semi-infinite powder bed is assumed in this model, as in Zhang and Faghri [9], however, an analysis of a finite thickness powder bed with constant heat flux may be found in Chen and Zhang [10]. It is assumed that the liquid phase is incompressible and the material properties are not affected by changes in temperature or pressure. The radiation and convection from the liquid surface are neglected so that the excess heat of the liquid must be dissipated in the form of conduction into the powder bed in order for the melt pool to resolidify.

2.1.1 Governing equations

2.1.1.1 Preheating stage

During preheating the powder bed can be described as a pure conduction problem. The heat conduction equation in the powder bed is

$$\frac{\partial T_s}{\partial t} = \alpha_s \frac{\partial^2 T_s}{\partial z^2}, \qquad z > 0, \ -\infty < t < t_m \tag{2}$$

subject to the boundary conditions

$$T_s \to T_i, \qquad z \to \infty, \ t > \infty \tag{3}$$

$$T_s = T_i, \qquad z \geq 0, \ t = -\infty \tag{4}$$

The heat flux at the surface is governed by

$$-k_s \frac{\partial T_s}{\partial z} = q''(t), \qquad z = 0, \ -\infty < t < t_m \tag{5}$$

where k_s is the effective conductivity of the unsintered powder bed and is related to the conductivities of the metal powder particles and the interstitial gas, k_p and k_g, as well as porosity, ε_s [17].

2.1.1.2 Melting with shrinkage stage

After melting has begun, $t \geq t_m$, the governing equation in the liquid phase is

$$\alpha_\ell \frac{\partial^2 T_\ell}{\partial z^2} = \frac{\partial T_\ell}{\partial t} + w \frac{\partial T_\ell}{\partial z}, \qquad s_0 < z < s(t), \ t_m < t < t_{sol} \tag{6}$$

where t_{sol} is the time at which melting ends and solidification begins, and w is the velocity in the liquid induced by the shrinkage of the powder bed, which plays an important role in heat transfer in the liquid region as demonstrated by an order of magnitude analysis in Ref. [9]. Equation (6) is subject to the following boundary condition

$$-k_\ell \frac{\partial T_\ell}{\partial z} = q''(t), \qquad z = s_0, \ t_m < t < t_{sol} \tag{7}$$

The conductivity of the liquid melt pool, k_ℓ, is obtained by

$$k_\ell = (1 - \varepsilon_\ell) k_p \tag{8}$$

Since the liquid is incompressible, the shrinkage velocity can be expressed by

$$w = \frac{ds_0}{dt}, \qquad s_0 < z < s(t), \ t_m < t < t_{sol}. \tag{9}$$

The governing equation for the solid phase (loose powder) after melting begins is

$$\frac{\partial T_s}{\partial t} = \alpha_s \frac{\partial^2 T_s}{\partial z^2}, \qquad s(t) < z,\ t_m < t < t_{sol}\,. \tag{10}$$

At the solid-liquid interface the temperature is

$$T_\ell(z,t) = T_s(z,t) = T_m, \qquad z = s(t),\ t_m < t < t_{sol} \tag{11}$$

and the energy balance can be expressed as

$$k_s \frac{\partial T_s}{\partial z} - k_\ell \frac{\partial T_\ell}{\partial z} = (1-\varepsilon_s)\phi\rho_L h_{sl} \frac{ds}{dt}, \qquad z = s(t),\ t_m < t < t_{sol}\,. \tag{12}$$

Based on the conservation of mass at the solid-liquid interface the shrinkage velocity, w, and the solid-liquid interface velocity, ds/dt, have the relationship

$$w = \frac{\varepsilon_s - \varepsilon_\ell}{1-\varepsilon_\ell} \frac{ds}{dt}\,. \tag{13}$$

2.1.1.3 Resolidification stage

As the heat flux at the surface of the powder bed decreases, heating of the powder bed will decrease and melting will begin to slow and eventually stop. The point of time at which melting of the powder bed stops is also the point at which solidification begins, t_{sol}. At the time t_{sol} the shrinkage reaches its maximum value and thus the location of the surface of the powder bed is unchanged during the solidification time period meaning that $s_0 = const$ and $w = 0$.

Taking these two factors into consideration the governing equations after solidification begins are

$$\frac{\partial T_\ell}{\partial t} = \alpha_\ell \frac{\partial^2 T_\ell}{\partial z^2}, \qquad s_0 > z > s(t),\ t > t_{sol} \tag{14}$$

$$-k_\ell \frac{\partial T_\ell}{\partial z} = q''(t), \qquad z = s_0,\ t > t_{sol} \tag{15}$$

$$\frac{\partial T_s}{\partial t} = \alpha_s \frac{\partial^2 T_s}{\partial z^2}, \qquad z > s(t = t_{sol}),\ t > t_{sol} \tag{16}$$

$$\frac{\partial T_r}{\partial t} = \alpha_r \frac{\partial^2 T_r}{\partial z^2}, \qquad s(t) < z < s(t = t_{sol}),\ t > t_{sol} \tag{17}$$

$$T_\ell(z,t) = T_r(z,t) = T_m, \qquad z = s(t),\ t > t_s \tag{18}$$

$$k_r \frac{\partial T_r}{\partial z} - k_\ell \frac{\partial T_\ell}{\partial z} = (1-\varepsilon_\ell)\phi\rho_L h_{sl} \frac{ds}{dt}, \qquad z = s(t),\ t > t_{sol} \tag{19}$$

$$T_r(z,t) = T_s(z,t), \qquad z = s(t = t_{sol}),\ t > t_{sol} \tag{20}$$

$$k_r \frac{\partial T_r}{\partial z} = k_s \frac{\partial T_s}{\partial z}, \qquad z = s(t = t_{sol}),\ t > t_{sol} \tag{21}$$

$$\frac{\partial T_r}{\partial t} = \frac{\partial T_s}{\partial t}, \qquad z = s(t = t_{sol}),\ t > t_{sol} \tag{22}$$

where the subscript r denotes the resolidified part, which is simply the resolidified liquid phase ℓ. It is assumed that the properties of the resolidified region are the same as that of the liquid region (e.g., $k_r = k_\ell$).

2.1.2 Nondimensional governing equations

By defining the following dimensionless variables

$$\begin{aligned}
&\tau = \frac{t}{t_p},\ \ \tau_{sol} = \frac{t_{sol}}{t_p},\ \ \tau_m = \frac{t_m}{t_p},\ \ Z = \frac{z}{\sqrt{\alpha_p t_p}},\ \ S = \frac{s}{\sqrt{\alpha_p t_p}},\ \ S_0 = \frac{s_0}{\sqrt{\alpha_p t_p}} \\
&W = \frac{t_p w}{\sqrt{\alpha_p t_p}},\ \ K_g = \frac{k_g}{k_p},\ \ K_s = \frac{k_s}{k_p(1-\varepsilon_s)},\ \ \bar{\alpha}_s = \frac{\alpha_s}{\alpha_p},\ \ Ste = q_0'' \frac{\sqrt{\alpha_p t_p}}{\alpha_p \phi h_{sl} \rho_L} \\
&\theta = \frac{\left(\rho c_p\right)_p}{\phi h_{sl}\rho_L}(T - T_m),\ \ \mathrm{S}c = \frac{\left(\rho c_p\right)_p}{\phi h_{sl}\rho_L}(T_m - T_i)
\end{aligned} \tag{23}$$

the following dimensionless governing equations will be obtained.

2.1.2.1 Preheating stage

$$\frac{\partial \theta_s}{\partial \tau} = \overline{\alpha}_s \frac{\partial^2 \theta_s}{\partial Z^2}, \qquad Z > 0,\ -\infty < \tau < \tau_m \tag{24}$$

$$\frac{\partial \theta_s}{\partial Z} = -\frac{Ste \cdot e^{-\tau^2}}{K_s(1-\varepsilon_s)}, \qquad Z = 0,\ -\infty < \tau < \tau_m \tag{25}$$

$$\theta_s = -Sc, \qquad Z \geq 0,\ \tau = -\infty \tag{26}$$

$$\theta_s \to -Sc, \qquad Z \to \infty,\ \tau > -\infty \tag{27}$$

2.1.2.2 Melting with shrinkage stage

$$\frac{\partial \theta_\ell}{\partial \tau} + W \frac{\partial \theta_\ell}{\partial Z} = \frac{\partial^2 \theta_\ell}{\partial Z^2}, \qquad \mathrm{S}_0 < Z < S,\ \tau_m < \tau < \tau_{sol} \tag{28}$$

$$W = \frac{dS_0}{d\tau}, \qquad Z = S_0,\ \tau_m < \tau < \tau_{sol} \tag{29}$$

$$\frac{\partial \theta_\ell}{\partial Z} = -\frac{Ste \cdot e^{-\tau^2}}{(1-\varepsilon_\ell)}, \qquad Z = S_0,\ \tau_m < \tau < \tau_{sol} \tag{30}$$

$$\frac{\partial \theta_s}{\partial \tau} = \overline{\alpha}_s \frac{\partial^2 \theta_s}{\partial Z^2}, \qquad S(\tau) < Z < \infty \tag{31}$$

$$\theta_\ell(Z,\tau) = \theta_s(Z,\tau) = 0, \qquad Z = S(\tau),\ \tau_m < \tau < \tau_{sol} \tag{32}$$

$$K_s \frac{\partial \theta_s}{\partial Z} - \frac{1-\varepsilon_\ell}{1-\varepsilon_s} \frac{\partial \theta_\ell}{\partial Z} = \frac{dS}{d\tau}, \qquad Z = S(\tau),\ \tau_m < \tau < \tau_{sol} \tag{33}$$

$$W = \frac{\varepsilon_s - \varepsilon_\ell}{1-\varepsilon_\ell} \frac{dS}{d\tau}, \qquad \mathrm{S}_0 < Z < S(\tau),\ \tau_m < \tau < \tau_{sol} \tag{34}$$

2.1.2.3 Resolidification stage

$$\frac{\partial \theta_\ell}{\partial \tau} = \frac{\partial^2 \theta_\ell}{\partial Z^2}, \qquad \mathrm{S}_0 < Z < S(\tau),\ \tau > \tau_{sol} \tag{35}$$

$$\frac{\partial \theta_\ell}{\partial Z} = -\frac{Ste \cdot e^{-\tau^2}}{1-\varepsilon_\ell}, \qquad Z = S_0,\ \tau > \tau_{sol} \tag{36}$$

$$\frac{\partial \theta_s}{\partial \tau} = \bar{\alpha}_s \frac{\partial^2 \theta_s}{\partial Z^2}, \qquad S(\tau = \tau_{sol}) < Z,\ \tau > \tau_{sol} \tag{37}$$

$$\frac{\partial \theta_r}{\partial \tau} = \frac{\partial^2 \theta_r}{\partial Z^2}, \qquad \mathrm{S}(\tau = \tau_{\mathrm{sol}}) < Z < S(\tau),\ \tau > \tau_{sol} \tag{38}$$

$$\theta_\ell(Z,\tau) = \theta_r(Z,\tau) = 0, \qquad Z = S(\tau),\ \tau > \tau_{sol} \tag{39}$$

$$\frac{\partial \theta_r}{\partial Z} - \frac{\partial \theta_\ell}{\partial Z} = \frac{dS}{d\tau}, \qquad Z = S(\tau),\ \tau > \tau_{sol} \tag{40}$$

$$\theta_r(Z,\tau) = \theta_s(Z,\tau), \qquad Z = S(\tau = \tau_{sol}),\ \tau > \tau_{sol} \tag{41}$$

$$\frac{\partial \theta_r}{\partial Z} = K_s \frac{1-\varepsilon_s}{1-\varepsilon_\ell} \frac{\partial \theta_s}{\partial Z}, \qquad Z = S(\tau = \tau_{sol}),\ \tau > \tau_{sol} \tag{42}$$

$$\frac{\partial \theta_r}{\partial \tau} = \frac{\partial \theta_s}{\partial \tau}, \qquad Z = S(\tau = \tau_{sol}),\ \tau > \tau_{sol} \tag{43}$$

The solutions of all the above three stages will be obtained using the integral approximate method with second degree polynomial temperature profiles.

2.2 The integral approximate solution

When the surface of the powder bed is exposed to heat flux the heat will penetrate the surface and begin to conduct downward. The depth to which the heat flux has penetrated is called the thermal penetration depth, δ. Beyond this depth the temperature is equal to the initial powder bed temperature. Therefore, the following two dimensionless boundary conditions at the dimensionless thermal penetration depth, $\Delta = \delta / \sqrt{\alpha_p t_p}$, are valid:

$$\theta_s(Z) = -Sc, \qquad Z \geq \Delta(\tau),\ \tau > -\infty \tag{44}$$

$$\frac{\partial \theta_s}{\partial Z}=0, \qquad Z \geq \Delta(\tau),\ \ \tau > -\infty \tag{45}$$

2.2.1 Solution for the preheating stage

By integrating both sides of Eq. (24) with respect to Z in the interval of $(0,\Delta)$ one obtains

$$\frac{1}{\bar{\alpha}_s}\int_0^{\Delta}\frac{\partial \theta_s}{\partial \tau}dZ = \left.\frac{\partial \theta_s}{\partial Z}\right|_0^{\Delta}. \tag{46}$$

Using Leibniz's Rule to yield

$$\int_0^{\Delta}\frac{\partial \theta_s}{\partial \tau}dZ = \frac{\partial}{\partial \tau}\int_0^{\Delta}\theta_s dZ - \theta_s(\Delta)\frac{\partial \Delta}{\partial \tau} \tag{47}$$

and substituting Eq. (47) into Eq. (46) and simplifying results in

$$\frac{1}{\bar{\alpha}_s}\left[\frac{\partial}{\partial \tau}\int_0^{\Delta}\theta_s dZ - \theta_s(\Delta)\frac{\partial \Delta}{\partial \tau}\right] = \left.\frac{\partial \theta_s}{\partial Z}\right|_{\Delta} - \left.\frac{\partial \theta_s}{\partial Z}\right|_0 \tag{48}$$

Applying the boundary conditions given by Eq. (27) and Eq. (44) and substituting Eq. (25) the result is

$$\frac{1}{\bar{\alpha}_s}\left[\frac{\partial}{\partial \tau}\int_0^{\Delta}\theta_s dZ + Sc\frac{\partial \Delta}{\partial \tau}\right] = \frac{Ste\cdot e^{-\tau^2}}{K_s(1-\varepsilon_s)} \tag{49}$$

Assuming that the temperature distribution profile is a second order polynomial of the form

$$\theta_s(Z,\tau) = A_s + B_s Z + C_s Z^2, \qquad \tau < \tau_m \tag{50}$$

and solving for A_s, B_s, and C_s using the boundary conditions of Eqs. (27), (25), and (44) yields

$$A_s = -Sc + \frac{Ste\cdot e^{-\tau^2}\cdot\Delta}{2K_s(1-\varepsilon_s)} \qquad B_s = \frac{-Ste\cdot e^{-\tau^2}}{K_s(1-\varepsilon_s)} \qquad C_s = \frac{Ste\cdot e^{-\tau^2}}{2\Delta K_s(1-\varepsilon_s)}$$

Substituting these coefficients into Eq. (50) gives a temperature profile of

$$\theta_s(Z,\tau) = -Sc + \frac{Ste \cdot e^{-\tau^2}}{2\Delta K_s(1-\varepsilon_s)}\left(\Delta - Z\right)^2, \qquad \tau < \tau_m \tag{51}$$

which can be substituted into Eq. (49) to find

$$\frac{\partial}{\partial \tau}\left[e^{-\tau^2}\Delta^2\right] = 6\bar{\alpha}_s e^{-\tau^2} \tag{52}$$

Integrating both sides of Eq. (52) from $-\infty$ to τ yields

$$e^{-\tau^2}\Delta^2 = 6\bar{\alpha}_s \int_{-\infty}^{\tau} e^{-\tau^2} d\tau \tag{53}$$

The integral of the exponential function results in an error function term. Therefore the thermal penetration depth in the powder bed is given by

$$\Delta = \sqrt{3\sqrt{\pi}\bar{\alpha}_s e^{\tau^2}\left[1 + erf(\tau)\right]}, \qquad \tau < \tau_m \tag{54}$$

When melting begins at time $\tau = \tau_m$ the temperature of the powder bed surface will be equal to the melting point of the low melting point powder, $\theta_s = 0$, i.e.,

$$\theta_s(Z=0, \tau=\tau_m) = 0 = -Sc + \frac{Ste \cdot e^{-\tau_m^2} \cdot \Delta_m}{2K_s(1-\varepsilon_s)} \tag{55}$$

The thermal penetration depth at the end of preheating can be obtained from Eq. (54)

$$\Delta_m = \sqrt{3\sqrt{\pi}\bar{\alpha}_s e^{\tau_m^2}\left[1 + erf(\tau_m)\right]} \tag{56}$$

Equations (55) and (56) give two equations for two unknowns which can be solved to find

$$\tau_m = \pm\sqrt{\ln\left[\frac{3\sqrt{\pi}\bar{\alpha}_s Ste^2\left[1 + erf(\tau_m)\right]}{4Sc^2 K_s{}^2(1-\varepsilon_s)^2}\right]} \tag{57}$$

Due to the error function expression, τ_m must be solved for in an iterative fashion. If the values of τ_m are close to zero then they must be examined carefully to determine which value to use.

2.2.2 Solution for the melting stage

2.2.2.1 Loose powder region

Although preheating ends when the temperature at the surface of the powder bed meets the melting point of the low melting point powder, the solid solution is still needed in the region from the solid-liquid interface to the thermal penetration depth where the temperature is elevated but melting has not begun. The following procedure is nearly identical to the preheating solution, the principal change being the limits of integration.

Integrating both sides of Eq. (31) gives

$$\frac{1}{\bar{\alpha}_s}\int_S^{\Delta}\frac{\partial\theta_s}{\partial\tau}dZ = \left.\frac{\partial\theta_s}{\partial Z}\right|_S^{\Delta} \tag{58}$$

Applying Leibniz's Rule to the left hand side of Eq. (58) yields

$$\int_S^{\Delta}\frac{\partial\theta_s}{\partial\tau}dZ = \frac{\partial}{\partial\tau}\int_S^{\Delta}\theta_s dZ - \theta_s(\Delta)\frac{\partial\Delta}{\partial\tau} + \theta_s(S)\frac{\partial S}{\partial\tau} \tag{59}$$

which may be substituted into Eq. (58). Applying the boundary conditions given by Eqs. (27), (44), and (32) gives

$$\frac{-1}{\bar{\alpha}_s}\left[\frac{\partial}{\partial\tau}\int_S^{\Delta}\theta_s dZ + Sc\frac{\partial\Delta}{\partial\tau}\right] = \left.\frac{\partial\theta_s}{\partial Z}\right|_S \tag{60}$$

Assuming that the temperature distribution profile is a second order polynomial of the form

$$\theta_s(Z,\tau) = A_s + B_s(Z-S) + C_s(Z-S)^2, \qquad \tau > \tau_m \tag{61}$$

and solving for A_s, B_s, and C_s using the boundary conditions given by Eqs. (27), (44), and (32) gives

$$A_s = 0 \qquad B_s = \frac{-2Sc}{(\Delta - S)} \qquad C_s = \frac{Sc}{(\Delta - S)^2}$$

The assumed nondimensional temperature profile is thus

$$\theta_s(Z,\tau) = Sc\left[\left(\frac{\Delta - Z}{\Delta - S}\right)^2 - 1\right] \tag{62}$$

Substituting Eq. (62) into Eq. (60) yields

$$\frac{6\overline{\alpha}_s}{\Delta - S} = \frac{\partial \Delta}{\partial \tau} + 2\frac{\partial S}{\partial \tau} \tag{63}$$

which describes the relationship between the location of the solid-liquid interface and the thermal layer thickness. It is subject to the initial conditions

$$\Delta = \Delta_m, \quad \tau = \tau_m \tag{64}$$

$$S = 0, \quad \tau = \tau_m . \tag{65}$$

2.2.2.2 Liquid region

Integrating both sides of Eq. (28) and applying Leibniz's Rule gives

$$\left.\frac{\partial \theta_l}{\partial Z}\right|_S - \left.\frac{\partial \theta_l}{\partial Z}\right|_{S_0} = \frac{\partial}{\partial \tau}\int_{S_0}^{S} \theta_l \partial Z + \theta_l(S_0)\frac{\partial S_0}{\partial \tau} - \theta_l(S)\frac{\partial S}{\partial \tau} + W\left[\theta_l(S) - \theta_l(S_0)\right] \tag{66}$$

Applying the boundary conditions given from Eqs. (30) and (32) and recalling Eq. (29) reduces Eq. (66) to

$$\frac{\partial}{\partial \tau}\int_{S_0}^{S} \theta_l dZ - \frac{Ste \cdot e^{-\tau^2}}{1-\varepsilon_l} = \left.\frac{\partial \theta_l}{\partial Z}\right|_S \tag{67}$$

At this point a temperature distribution of the form

$$\theta_l(Z,\tau) = A_l + B_l\left(\frac{Z-S}{S}\right) + C_l\left(\frac{Z-S}{S}\right)^2 \tag{68}$$

may be assumed, however, the boundary conditions of Eqs. (30) and (32) will not be enough more to determine all three coefficients of the polynomial. We will find the third boundary condition by differentiating Eq. (32) and using the relation

$$d\theta_l = \frac{\partial\theta_l}{\partial Z}dZ + \frac{\partial\theta_l}{\partial\tau}d\tau = 0, \qquad Z = S(\tau),\ \tau > \tau_m \tag{69}$$

$$0 = \frac{\partial\theta_l}{\partial Z}\frac{dZ}{d\tau} + \frac{\partial\theta_l}{\partial\tau}, \qquad Z = S(\tau),\ \tau > \tau_m \tag{70}$$

$$0 = \left.\frac{\partial\theta_l}{\partial Z}\right|_S \left.\frac{dZ}{d\tau}\right|_S + \left.\frac{\partial\theta_l}{\partial\tau}\right|_S \tag{71}$$

$$0 = \frac{\partial\theta_l}{\partial Z}\frac{dS}{d\tau} + \frac{\partial\theta_l}{\partial\tau}, \qquad Z = S(\tau),\ \tau > \tau_m \tag{72}$$

Substituting Eqs. (28) and (33) into Eq. (72) gives

$$0 = K_s\left.\frac{\partial\theta_s}{\partial Z}\right|_S \left.\frac{\partial\theta_l}{\partial Z}\right|_S - \frac{1-\varepsilon_l}{1-\varepsilon_s}\left(\left.\frac{\partial\theta_l}{\partial Z}\right|_S\right)^2 + \left.\frac{\partial^2\theta_l}{\partial Z^2}\right|_S - W\left.\frac{\partial\theta_l}{\partial Z}\right|_S \tag{73}$$

The $\frac{\partial\theta_s}{\partial Z}$ term can be replaced by a manipulation of Eq. (62) to give

$$0 = -\frac{1-\varepsilon_l}{1-\varepsilon_s}\left(\left.\frac{\partial\theta_l}{\partial Z}\right|_S\right)^2 + \left[\frac{-2ScK_s}{\Delta - S} - W\right]\left.\frac{\partial\theta_l}{\partial Z}\right|_S + \left.\frac{\partial^2\theta_l}{\partial Z^2}\right|_S \tag{74}$$

A combination of Eqs. (33), (34), and the derivative of Eq. (62) will be used to eliminate W, yielding the final boundary condition of

$$0 = -\left(\left.\frac{\partial\theta_l}{\partial Z}\right|_S\right)^2 - \frac{1-\varepsilon_s}{1-\varepsilon_l}\frac{2ScK_s}{\Delta - S}\left.\frac{\partial\theta_l}{\partial Z}\right|_S + \left.\frac{\partial^2\theta_l}{\partial Z^2}\right|_S \tag{75}$$

Now that there are three boundary conditions for the three unknown coefficients it is possible to find the temperature profile. By substituting Eq. (68) into Eq. (32) it is clear that $A_l = 0$. Continuing in this manner, Eq. (68), differentiated one time, is substituted into Eq. (30) to obtain B_l. Keeping in mind the relation $S_0 - S = -S\frac{1-\varepsilon_s}{1-\varepsilon_l}$, which can be obtained by combining Eqs. (29) and (34) and integrating both sides gives

$$B_l = \frac{-S \cdot Ste \cdot e^{-\tau^2}}{1-\varepsilon_l} + 2C_l \frac{1-\varepsilon_s}{1-\varepsilon_l} \tag{76}$$

Substituting A_l and B_l into the assumed temperature profile in the liquid phase yields

$$\theta_l(Z,\tau) = \left[\frac{-S \cdot Ste \cdot e^{-\tau^2}}{1-\varepsilon_l} + 2C_l \frac{1-\varepsilon_s}{1-\varepsilon_l}\right]\left(\frac{Z-S}{S}\right) + C_l\left(\frac{Z-S}{S}\right)^2 \tag{77}$$

To find C_l, substitute the differentials of the assumed liquid temperature profile into Eq. (74) to give

$$0 = -\frac{B_l^2}{S^2} - \frac{1-\varepsilon_s}{1-\varepsilon_l}\frac{2ScK_s}{\Delta - S}\frac{B_l}{S} + \frac{2C_l}{S^2} \tag{78}$$

By substituting the known coefficients B_l and collect terms for C_l a second order polynomial for C_l is obtained.

$$\begin{aligned} 0 = {} & C_l^2\left[-4\frac{(1-\varepsilon_s)^2}{(1-\varepsilon_l)^2}\right] \\ & + C_l\left[2 + 4Ste \cdot e^{-\tau^2}\frac{1-\varepsilon_s}{(1-\varepsilon_l)^2}S + \frac{-4ScK_s}{(\Delta - S)}\frac{(1-\varepsilon_s)^2}{(1-\varepsilon_l)^2}S\right] \\ & + \left[\frac{-Ste^2 \cdot e^{-2\tau^2}}{(1-\varepsilon_l)^2}S^2 + Ste \cdot e^{-\tau^2}\frac{2ScK_s}{(\Delta - S)}\frac{(1-\varepsilon_s)}{(1-\varepsilon_l)^2}S^2\right] \end{aligned} \tag{79}$$

The roots of this polynomial will give two possible temperature profiles, only one of which will be both concave down and satisfy the necessary boundary conditions.

Now that the temperature distributions for both phases are known the next task is now to find the locations of the solid-liquid interface, S, and the thermal penetration depth, Δ. To do this substitute Eq. (60) and Eq. (67) into Eq. (33) to obtain

$$\frac{-K_s}{\bar{\alpha}_s}\left[\frac{\partial}{\partial\tau}\int_S^{\Delta}\theta_s dZ + Sc\frac{\partial\Delta}{\partial\tau}\right] - \frac{1-\varepsilon_l}{1-\varepsilon_s}\left[\frac{\partial}{\partial\tau}\int_{S_0}^{S}\theta_l dZ - \frac{Ste\cdot e^{-\tau^2}}{1-\varepsilon_l}\right] = \frac{dS}{d\tau}, \quad Z = S(\tau), \quad \tau > \tau_m \tag{80}$$

which can be integrated with respect to τ over the interval (τ_m, τ) and simplified to yield

$$S = \frac{-K_s}{\bar{\alpha}_s}\left[\int_S^{\Delta}\theta_s dZ - \int_0^{\Delta_m}\theta_s dZ + Sc(\Delta-\Delta_m)\right] - \frac{1-\varepsilon_l}{1-\varepsilon_s}\int_{S_0}^{S}\theta_l dZ + \frac{Ste\sqrt{\pi}}{2(1-\varepsilon_s)}[erf(\tau)-erf(\tau_m)] \tag{81}$$

The integrals of the temperature profiles in Eqs. (51), (62), and (77) are

$$\int_S^{\Delta}\theta_s dZ = \frac{2}{3}Sc(S-\Delta) \tag{82}$$

$$\int_0^{\Delta_m}\theta_s dZ = -\frac{2}{3}Sc\Delta_m \tag{83}$$

$$\int_{S_0}^{S}\theta_l dZ = \frac{1}{2}Ste\cdot e^{-\tau^2}\frac{(1-\varepsilon_s)^2}{(1-\varepsilon_l)^3}S^2 - \frac{2}{3}C\left(\frac{1-\varepsilon_s}{1-\varepsilon_l}\right)^3 S \tag{84}$$

which are substituted into Eq. (81) to find

$$\begin{aligned} 0 = {} & S^2\left[-\frac{1}{2}Ste\cdot e^{-\tau^2}\frac{1-\varepsilon_s}{(1-\varepsilon_l)^2}\right] \\ & + S\left[-1-\frac{2}{3}\frac{ScK_s}{\bar{\alpha}_s}+\frac{2}{3}C_l\left(\frac{1-\varepsilon_s}{1-\varepsilon_l}\right)^2\right] \\ & + \left[-\frac{1}{3}\frac{ScK_s}{\bar{\alpha}_s}(\Delta-\Delta_m)+\frac{Ste\sqrt{\pi}}{2(1-\varepsilon_s)}[erf(\tau)-erf(\tau_m)]\right] \end{aligned} \tag{85}$$

The roots of this polynomial will be the possible values of S, only one of which will be both positive and real. Integrating both sides of Eq. (63) with respect to τ to obtain

$$\Delta = \Delta_m - 2S + \int_{\tau_m}^{\tau} \frac{6\bar{\alpha}_s}{\Delta - S} d\tau \tag{86}$$

the final necessary equation. The right side of Eq. (86) must be evaluated using numerical integration. By solving Eqs. (86) and (85) the location of the solid-liquid interface and the thermal penetration depth will be obtained.

2.2.3 Solution for the resolidification stage

As the heat flux at the surface of the powder bed decreases melting will slow down and eventually stop. When melting stops the motion of the solid-liquid interface will reverse direction and begin to move back toward the surface of the powder bed as the melt pool solidifies. Since melting has stopped there is no longer a density change in the powder bed and shrinkage of the powder bed has ceased. The location of the liquid surface during the solidification period is fixed, meaning that $S_0 = const$ and $W = 0$. These factors will be taken into account during the solution of the solidification period.

2.2.3.1 Loose powder region

Integrating both sides of Eq. (37) and apply the boundary condition of Eq. (45) gives the integral equation in the loose powder

$$\frac{-1}{\bar{\alpha}_s}\left[\frac{\partial}{\partial \tau}\int_{S_{sol}}^{\Delta} \theta_s dZ + Sc\frac{\partial \Delta}{\partial \tau}\right] = \left.\frac{\partial \theta_s}{\partial Z}\right|_{S_{sol}} \tag{87}$$

where S_{sol} is the location of the solid-liquid interface at the time $\tau = \tau_{sol}$.

Assuming a second degree polynomial of the same form as Eq. (61) and applying the boundary conditions of Eqs. (44) and (45) to eliminate two of the three coefficients, we can solve for B_s and C_s easily if we assume for a moment that A_s is known.

$$B_s = \frac{-2(A_s + Sc)}{\Delta - S_{sol}} \qquad C_s = \frac{A_s + Sc}{(\Delta - S_{sol})^2} \tag{88}$$

The temperature in the solid, unsintered powder then becomes

$$\theta_s(Z,\tau) = A_s + \frac{-2(A_s + Sc)}{\Delta - S_{sol}}(Z - S_{sol}) + \frac{A_s + Sc}{(\Delta - S_{sol})^2}(Z - S_{sol})^2, \qquad S_{sol} < Z < \Delta(\tau) \tag{89}$$

The thermal penetration depth can be found by integrating Eq. (87) once from τ_{sol} to τ. Using the assumed temperature distribution of Eq. (89) to evaluate the integral of θ_s from S_{sol} to Δ one obtains

$$\Delta(\tau) = \frac{6\bar{\alpha}_s}{A_s + Sc}\int_{\tau_{sol}}^{\tau} \frac{A_s + Sc}{\Delta - S_{sol}}\,d\tau + \frac{A_s S_{sol} + Sc\Delta_{sol}}{A_s + Sc}, \qquad \tau_{sol} < \tau < \tau_{final} \tag{90}$$

2.2.3.2 Resolidified region

The resolidified region is simply the portion of the melt pool that has resolidified. By integrating Eq. (38) once and applying the boundary conditions of Eqs. (39) and $S_{sol} = const$ the integral energy equation for the resolidified region becomes

$$\frac{\partial}{\partial \tau}\int_{S}^{S_{sol}} \theta_r\,dZ = \left.\frac{\partial \theta_r}{\partial Z}\right|_{S_{sol}} - \left.\frac{\partial \theta_r}{\partial Z}\right|_{S}, \qquad S < Z < S_{sol} \tag{91}$$

By assuming a second degree polynomial for the temperature distribution and applying the boundary conditions of Eqs. (39), (41), and (42), the coefficients of the temperature profile in the resolidified region are

$$A_r = 0$$
$$B_r = \frac{2A_s}{S_{sol} - S} + \frac{2K_s(A_s + Sc)}{\Delta - S_{sol}} \frac{1-\varepsilon_s}{1-\varepsilon_l} \tag{92}$$
$$C_r = \frac{-A_s}{(S_{sol} - S)^2} - \frac{2K_s(A_s + Sc)}{(\Delta - S_{sol})(S_{sol} - S)} \frac{1-\varepsilon_s}{1-\varepsilon_l}$$

where A_s is still unknown at this point. The assumed temperature profile is thus

$$\theta_r(Z) = \left[\frac{2A_s}{S_{sol} - S} + \frac{2K_s(A_s + Sc)}{\Delta - S_{sol}} \frac{1-\varepsilon_s}{1-\varepsilon_l} \right](Z - S) + \left[\frac{-A_s}{(S_{sol} - S)^2} - \frac{2K_s(A_s + Sc)}{(\Delta - S_{sol})(S_{sol} - S)} \frac{1-\varepsilon_s}{1-\varepsilon_l} \right](Z - S)^2, \qquad S(\tau) < Z < S_{sol} \tag{93}$$

To determine the coefficient A_s, the temperature at $Z = S_{sol}$, a combination of the sixth and final boundary condition, Eq. (43), and Eqs. (37) and (38) will be used to give

$$2C_r = \bar{\alpha}_s 2C_s \tag{94}$$

By substituting the known values for C_r and C_s into (94) one obtains

$$A_s = \frac{2ScK_s(1-\varepsilon_s)(S_{sol} - S)(\Delta - S_{sol}) + \bar{\alpha}_s Sc(S_{sol} - S)^2(1-\varepsilon_l)}{-(\Delta - S_{sol})^2(1-\varepsilon_l) - 2K_s(1-\varepsilon_s)(S_{sol} - S)(\Delta - S_{sol}) - \bar{\alpha}_s(S_{sol} - S)^2(1-\varepsilon_l)} \tag{95}$$

the final of the six coefficients.

2.2.3.3 Liquid region

The solution for the liquid region of the solidification stage can be obtained in a manner similar to the solution for the liquid region of the melting stage. Beginning with Eq. (35) , integrate both sides, use Leibniz's Rule, and apply the boundary conditions given by Eqs. (36) and (39) to get the integral energy equation in the melt pool

$$\frac{\partial}{\partial \tau} \int_{S_0}^{S} \theta_l dZ - \frac{Ste \cdot e^{-\tau^2}}{1-\varepsilon_l} = \left. \frac{\partial \theta_l}{\partial Z} \right|_S \tag{96}$$

Assuming that the temperature distribution in the liquid has the form of a second degree polynomial and applying the boundary conditions of Eqs. (36) and (39) will give us

$$A_l = 0$$
$$B_l = \frac{-Ste \cdot e^{-\tau^2}}{1-\varepsilon_l} S - \frac{2C_l}{S}(S_0 - S) \tag{97}$$

which are different than those of the melting period because S_0 is now constant. To find C_l a procedure similar to that of the melting period will be used. Combining Eqs. (72) and (35) will result in

$$0 = \left.\frac{\partial \theta_l}{\partial Z}\right|_S \frac{dS}{d\tau} + \left.\frac{\partial^2 \theta_l}{\partial Z^2}\right|_S \tag{98}$$

into which the assumed temperature profile in the liquid region, Eq. (68) will be substituted to find

$$0 = \frac{B_l}{S}\frac{dS}{d\tau} + \frac{2C_l}{S^2} \tag{99}$$

By substituting the assumed temperature profiles into Eq. (40) the relation

$$\frac{dS}{d\tau} = B_r - \frac{B_l}{S} \tag{100}$$

is obtained. Combining Eqs. (99) and (100) and collecting terms for C_l gives the second degree polynomial

$$0 = C_l^2\left[\frac{-4(S-S_0)^2}{S^2}\right] + C_l\left[2+\frac{4Ste\cdot e^{-\tau^2}}{1-\varepsilon_l}(S-S_0)+4(A_s+Sc)K_s\frac{1-\varepsilon_s}{1-\varepsilon_l}\frac{S_0-S}{S_{sol}-\Delta}-4A_s\frac{S_0-S}{S_{sol}-S}\right] + \left[\frac{-Ste^2\cdot e^{-2\tau^2}}{(1-\varepsilon_l)^2}S^2-\frac{2A_s}{1-\varepsilon_l}\frac{Ste\cdot e^{-\tau^2}}{S_{sol}-S}S^2+\frac{2K_s(Sc+A_s)}{S_{sol}-\Delta}Ste\cdot e^{-\tau^2}S^2\frac{1-\varepsilon_s}{(1-\varepsilon_l)^2}\right] \quad (101)$$

As in the melting stage, the roots of the C_l polynomial above will give two possible values for C_l, only one of which will be appropriate. The final temperature distribution in the liquid region is thus

$$\theta_l(Z,\tau) = \left[\frac{-Ste\cdot e^{-\tau^2}}{1-\varepsilon_l}S-\frac{2C_l}{S}(S_0-S)\right]\left(\frac{Z-S}{S}\right)+C_l\left(\frac{Z-S}{S}\right)^2 \quad (102)$$

In order to find how S changes with time, substitute the integral energy equations, Eqs. (91) and (96), into the energy balance equation at the resolidified part-liquid pool interface, Eq. (40).

$$\frac{dS}{d\tau} = \left.\frac{\partial\theta_r}{\partial Z}\right|_{S_{sol}} - \frac{\partial}{\partial\tau}\int_S^{S_{sol}}\theta_r dZ - \frac{\partial}{\partial\tau}\int_{S_0}^{S}\theta_l dZ + \frac{Ste\cdot e^{-\tau^2}}{1-\varepsilon_l} \quad (103)$$

Using the appropriate temperature profiles, integrate Eq. (103) from τ_{sol} to τ and collect terms for S to find the polynomial

$$
\begin{aligned}
0 = {} & S^4\left[\frac{-Ste\cdot e^{-\tau^2}}{2(1-\varepsilon_l)}+\frac{1-\varepsilon_s}{1-\varepsilon_l}\frac{K_s(A_s+Sc)}{3(S_{sol}-\Delta)}\right] \\
& +S^3\left[-1+\frac{2}{3}(A_s+C_l)+\frac{Ste\cdot e^{-\tau^2}}{(1-\varepsilon_l)}S_0-\frac{2}{3}\frac{1-\varepsilon_s}{1-\varepsilon_l}\frac{K_s(A_s+Sc)}{(S_{sol}-\Delta)}S_{sol}\right] \\
& +S^2\left[\begin{array}{l}
-2K_s\dfrac{1-\varepsilon_s}{1-\varepsilon_l}\displaystyle\int_{\tau_{sol}}^{\tau}\frac{A_s+Sc}{\Delta-S_{sol}}d\tau-2C_lS_0+S_{sol}+\frac{2C_{l,sol}}{3S_{sol}^{\ 2}}(S_0-S_{sol})^3 \\
\quad -\dfrac{2}{3}A_sS_{sol}-\dfrac{Ste\cdot e^{-\tau^2}}{2(1-\varepsilon_l)}S_0^{\ 2}+\dfrac{Ste\cdot e^{-\tau_{sol}^{\ 2}}}{2(1-\varepsilon_l)}(S_0-S_{sol})^2 \\
\quad +\dfrac{1}{3}\dfrac{1-\varepsilon_s}{1-\varepsilon_l}\dfrac{K_s(A_s+Sc)}{(S_{sol}-\Delta)}S_{sol}^{\ 2}+\dfrac{Ste\sqrt{\pi}}{2(1-\varepsilon_l)}\left[erf(\tau)-erf(\tau_{sol})\right]
\end{array}\right] \\
& +S^1\left[2C_lS_0^{\ 2}\right]+S^0\left[-\frac{2}{3}C_lS_0^{\ 3}\right]
\end{aligned}
\tag{104}
$$

one of the roots of which will be the location of the liquid-resolidified part interface.

$C_{l,sol}$ is simply the value of C_l at the time $\tau=\tau_{sol}$ or

$$
\begin{aligned}
0 = {} & C_{l,sol}^{\ 2}\left[\frac{-4(S_{sol}-S_0)^2}{S_{sol}^{\ 2}}\right] \\
& +C_{l,sol}\left[2+\frac{4Ste\cdot e^{-\tau_{sol}^{\ 2}}}{1-\varepsilon_l}(S_{sol}-S_0)+4ScK_s\frac{1-\varepsilon_s}{1-\varepsilon_l}\frac{S_0-S_{sol}}{S_{sol}-\Delta_{sol}}\right] \\
& +\left[\frac{-Ste^2\cdot e^{-2\tau_{sol}^{\ 2}}}{(1-\varepsilon_l)^2}S_{sol}^{\ 2}+S_{sol}^{\ 2}Ste\cdot e^{-\tau_{sol}^{\ 2}}\frac{1-\varepsilon_s}{(1-\varepsilon_l)^2}\frac{2ScK_s}{S_{sol}-\Delta_{sol}}\right]
\end{aligned}
\tag{105}
$$

Now that all of the necessary components to describe the location of the solid-liquid interface, the location of the liquid surface, and the temperature distributions for each time period have been found a computer simulation can be developed to give the results of the model.

2.3 Results and Discussion

The solutions of the preheating, melting, and resolidification stages have been derived in terms of nondimensional parameters. A computer code was written to simulate the

results of the model and the nondimensional values were varied to investigate the impact they would have on the sintering process. In all of the following simulations the material properties of the low melting point powder are that of Aluminum and the material properties of the high melting point powder are that of Titanium. The most important processing parameter is Stefan number. It is proportional to $q_0''\sqrt{t_p}$ [see Eq. (23)] and it can be affected by a change in either laser power or laser pulse width. The range of the Stefan number used in this study is obtained by using a peak heat flux on the order of $2\times10^6\ W\cdot m^{-2}$ and a laser pulse width of less than $0.50\ s$. The porosity of the liquid phase, ε_ℓ, was assumed to be 10%, meaning that not all of the interstitial gas in the powder bed is driven out during the melting stage. The porosity of the unsintered powder, ε_s, was assumed to be 40%. The value of ϕ, the percentage of low melting point powder in the powder bed, was chosen to be 40%. Resulting values of the nondimensional parameters can be found in the captions of the following figures.

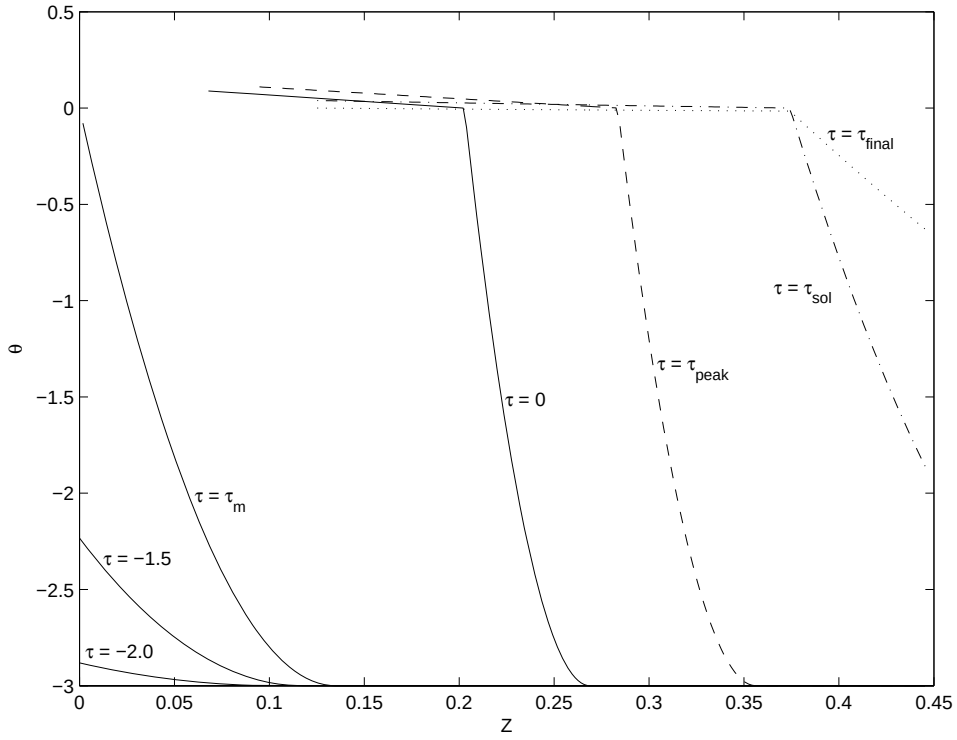

Figure 2.3.1 The temperature profile within the powder bed at various times.

($Ste = 0.6,\ Sc = 3.0,\ \varepsilon_s = 0.40,\ \varepsilon_\ell = 0.10,\ \phi = 0.40,\ \overline{\alpha}_s = 0.0081,\ K_s = 0.0081$**)**

Figure 2.3.1 shows the temperature profile within the powder bed at various times during a simulation for the baseline values of the dimensionless parameters. It shows an increase in temperature throughout the powder bed as the process continues. The line corresponding to $\tau = \tau_{peak}$ is the time at which the surface of the powder bed reaches its maximum temperature. Note that the temperature profile lines for $\tau \geq \tau_m$ do not extend all the way to $Z = 0$ due to shrinkage of the powder bed. The progression of the thermal penetration depth during the duration of the process can also be seen in the figure.

Figure 2.3.2 shows the change in temperature at the surface of the powder bed for different values of the Stefan number. The surface temperature increases as the heat flux

increases, with the peak surface temperature occurring after $\tau = 0$, the time at which maximum heat flux occurs. It can also be see in Fig. 2.3.2 that as the Stefan number increases the time at which melting begins decreases.

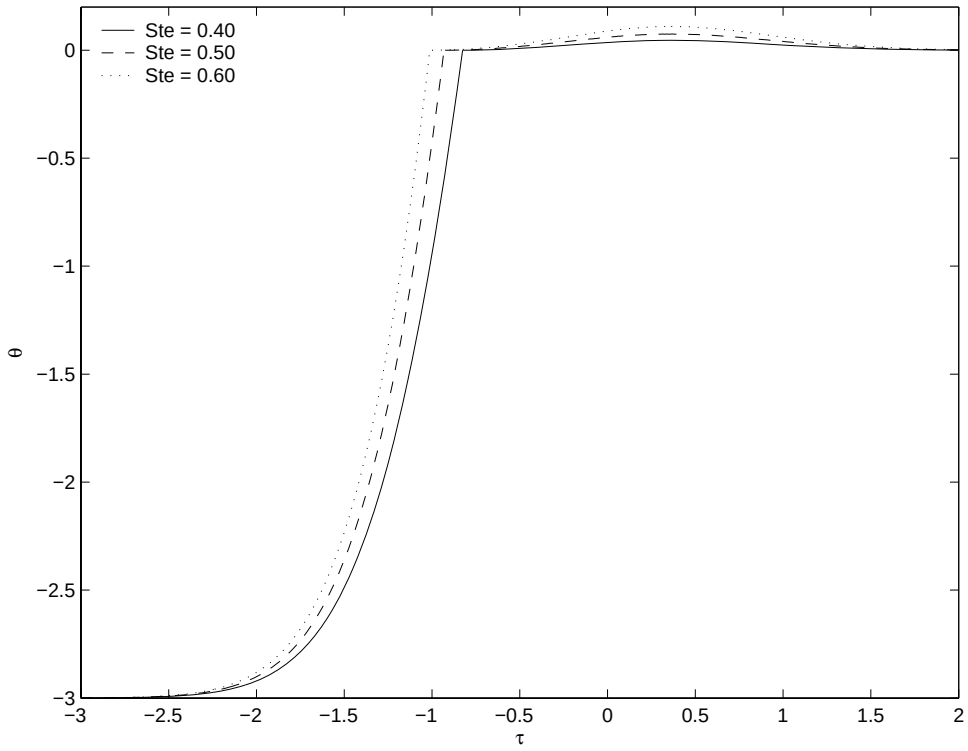

Figure 2.3.2 The surface temperature of the powder bed for various values of the Stefan number.

($Sc = 3.0,\ \varepsilon_s = 0.40,\ \varepsilon_\ell = 0.10,\ \phi = 0.40,\ \bar{\alpha}_s = 0.0081,\ K_s = 0.0081$**)**

Figure 2.3.3 shows the effect of the Stefan number, or the magnitude of the heat flux, on the locations of the solid-liquid interface, the liquid surface, and the thermal penetration depth. Obviously as the Stefan number increases the melt pool depth increases and the temperature of the melt pool surface increases, as evidenced by Fig.

2.3.2. A higher Stefan number will also result in more shrinkage, because more material will be melted, and a longer process time, because it will take longer for this increased quantity of melted powder to cool and resolidify.

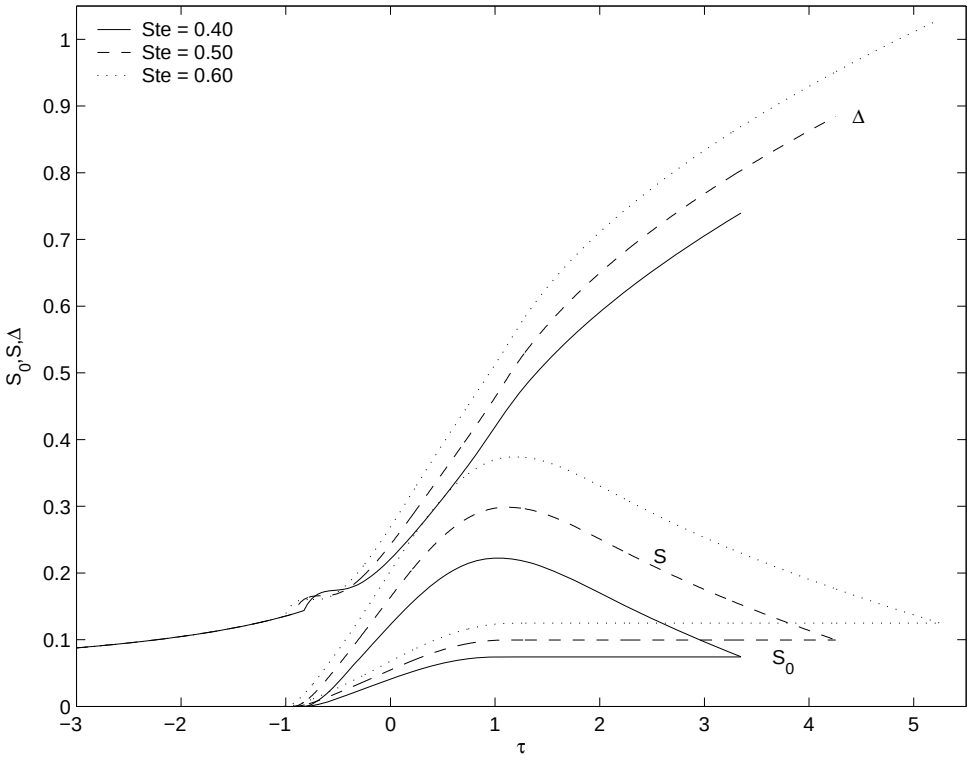

Figure 2.3.3 The location of the liquid surface, the solid-liquid interface, and the thermal penetration depth for various of the Stefan number.

($Sc = 3.0,\ \varepsilon_s = 0.40,\ \varepsilon_\ell = 0.10,\ \phi = 0.40,\ \bar{\alpha}_s = 0.0081,\ K_s = 0.0081$ **)**

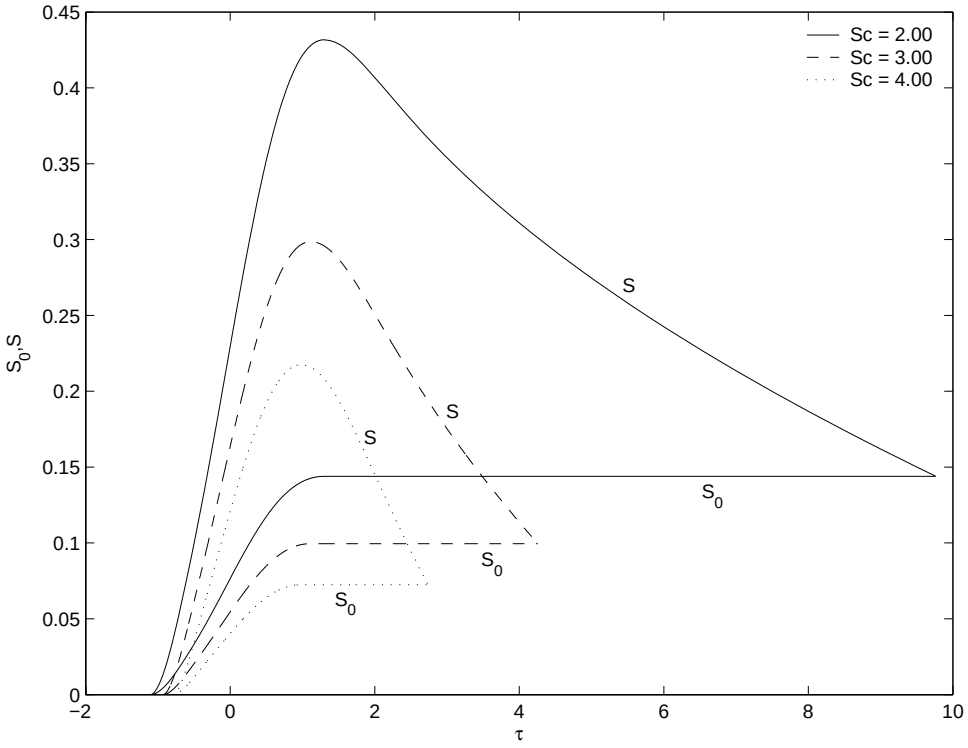

Figure 2.3.4 The effect of the subcooling parameter on the location of the liquid surface and the solid-liquid interface.

($Ste = 0.5,\ \varepsilon_s = 0.40,\ \varepsilon_\ell = 0.10,\ \phi = 0.40,\ \overline{\alpha}_s = 0.0081,\ K_s = 0.0081$**)**

Figure 2.3.4 shows the location of the liquid surface and the solid-liquid interface for the same Stefan number but different subcooling parameters. For $Sc = 4.0$ the laser beam pass makes a relatively shallow melt pool as compared to the hotter powder bed of $Sc = 3.0$. For the subcooling parameter of $Sc = 2.0$ the melt pool is very deep because the laser does not have to do nearly as much preheating. The higher the subcooling parameter, the greater the difference between the initial temperature of the powder bed and the melting point of the low melting point powder. Thus the higher the subcooling

parameter the more heat flux is needed to melt the powder and the longer it takes for melting to begin, which is confirmed by Fig. 2.3.4.

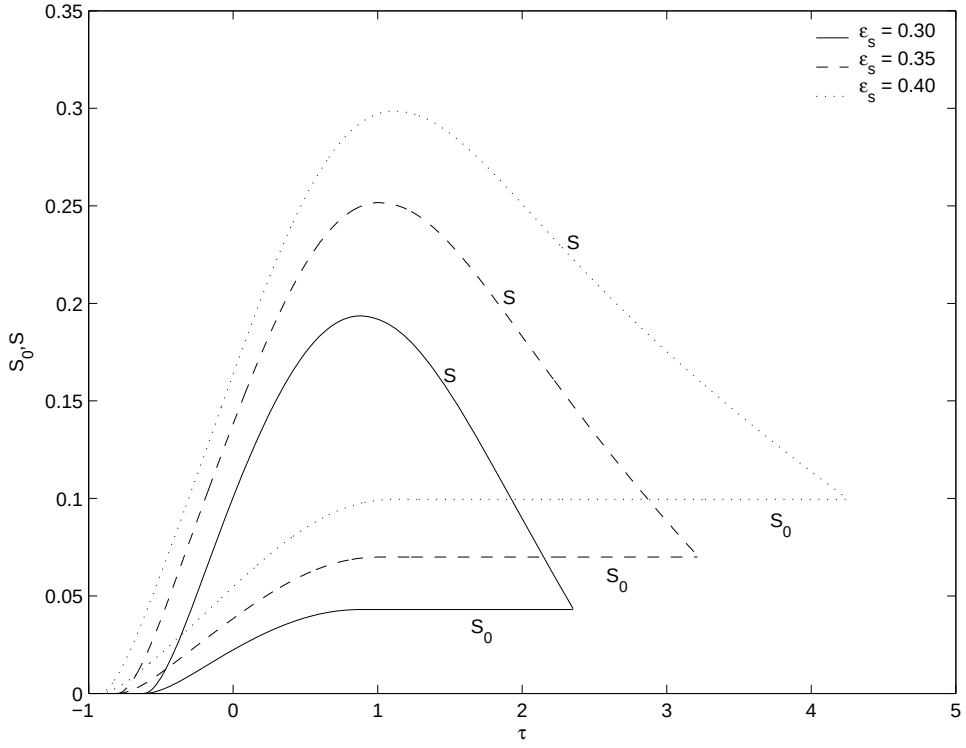

Figure 2.3.5 The effect of the porosity of the unsintered powder on the location of the liquid surface and the solid liquid interface.

($Ste = 0.5,\ Sc = 3.0,\ \varepsilon_\ell = 0.10,\ \phi = 0.40$ **)**

Obviously a powder bed that is very porous will experience a greater amount of shrinkage due to melting than one that is less porous, however, Fig. 2.3.5 shows that a very porous powder bed will also have a deeper melt pool and a longer process time. This is because as the porosity of the metal powder increases the effective thermal conductivity of the powder bed decreases. A very porous powder bed will reach the end

of the preheating period faster than a less porous one, and a greater volume of powder bed will be sintered, because the lower thermal conductivity will keep more of the heat flux at the surface of the powder bed, essentially not letting the heat flux penetrate the powder bed as quickly as a densely packed powder bed. This porosity will increase the process time significantly because in the model heat in the melt pool can only be lost via conduction of the heat deeper into the loose powder bed, not by radiation or convection at the surface.

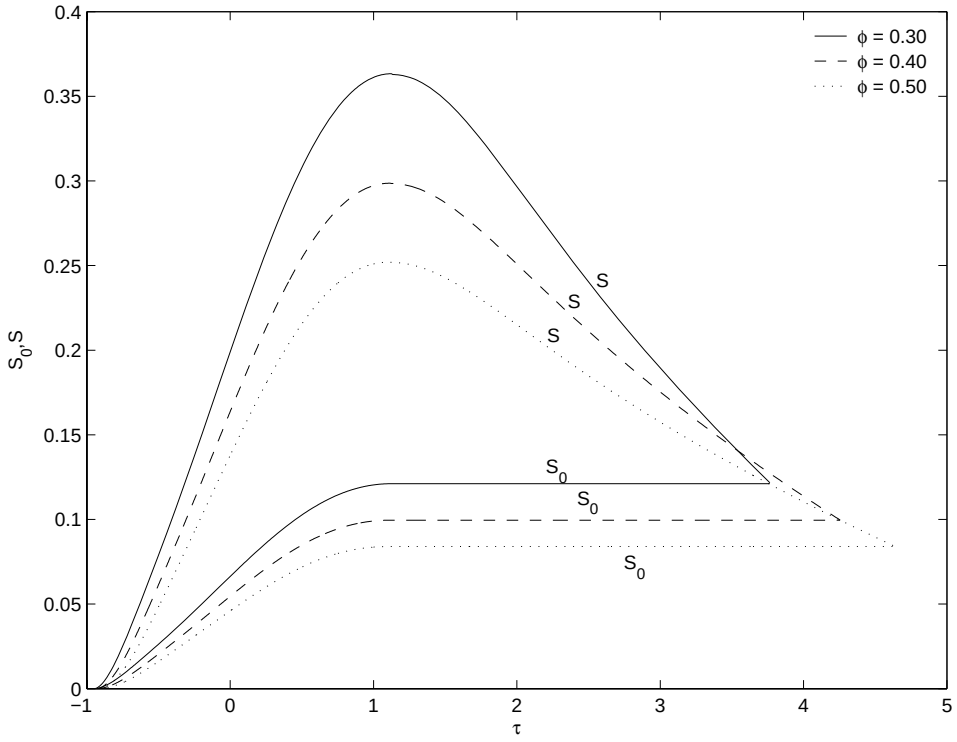

Figure 2.3.6 The effect of the fraction of low-melting-point powder on the location of the liquid surface and the solid-liquid interface. ($\varepsilon_s = 0.40,\ \varepsilon_\ell = 0.10$ **)**

Figure 2.3.6 shows the effect of a change in the fraction of low-melting point powder in the powder bed. The figure shows that as the fraction of low-melting-point powder in the powder bed increases the process time increases and the amount of melted material increases. This makes sense because if there is more low-melting-point powder in the powder bed then more material will be melted by the applied heat flux. More melted material means that more latent heat must be dissipated into the unsintered powder after the temporal Gaussian heat flux has decreased, hence an increase in process time.

2.4 Conclusion

Melting and solidification in a subcooled powder bed with temporal Gaussian heat flux was investigated analytically. It is clear that all process parameters have effects on the results of the SLS process but through nondimensionalization the number of independent parameters can be significantly reduced. As the Stefan number is increased the melt pool depth is also increased as well as the temperature of the melt pool surface and the overall process time. As subcooling of the powder bed increases more heat flux is needed to melt the powder, and thus the melt pool is shallower. It was found that a very porous powder bed will reach the end of the preheating period faster than a less porous one, a greater amount of material will be sintered, and the total process time will also increase. An increase in the fraction of low-melting-point powder will mainly increase the process time. The physical model and results of this investigation pave the way for further modeling of SLS processes with a pulsed laser.

Chapter 3. Heat transfer in a single powder particle

Heat conduction in a single subcooled powder particle subjected to temporal Gaussian heat flux from a laser beam will be modeled in this chapter. The diameter of the metal powder particle is much smaller than the diameter of the laser beam, which is in turn much smaller than the final desired part.

3.1 Physical model

The analysis of a single particle can be extended to the powder bed level by using an assumption based upon the optical penetration depth of the laser beam. Since the laser radiation penetrates the powder bed over a distance of several powder-sphere diameters, we can assume that multiple scattering of the radiation leads to a nearly homogeneous distribution of the heat flux within the optically penetrated layer. This assumption leads to an almost normal incidence of the radiation on the surfaces of the grains in the underlying layers. The physical model of melting and resolidification is shown in Fig. 3.1.1. Due to symmetry of the spherical particle in the θ and ϕ directions the model can be assumed to be one-dimensional in the r direction.

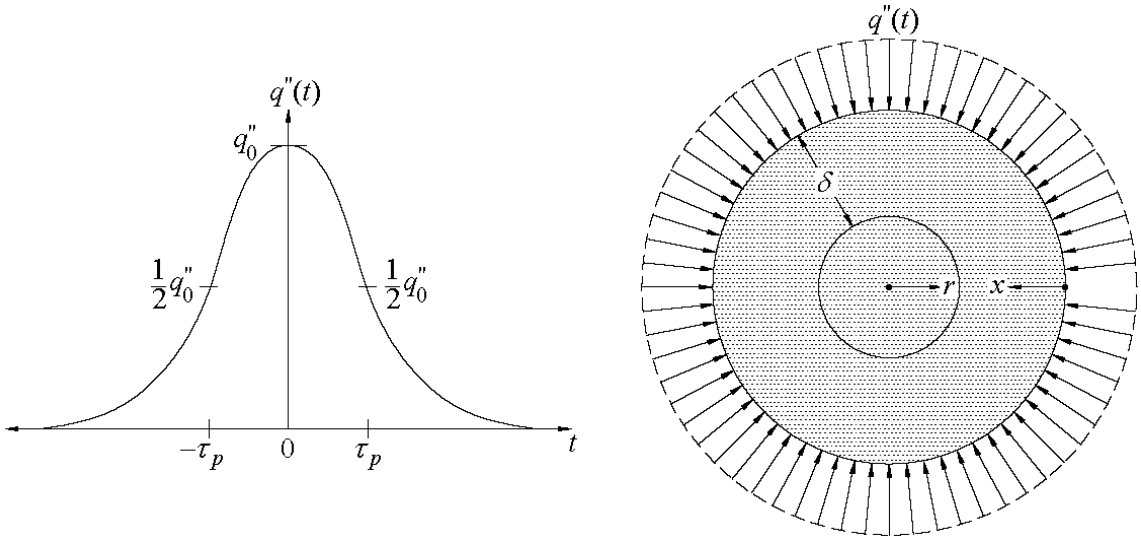

Figure 3.1.1 The physical model.

The initial temperature of the powder particle is well below its melting point. The origin of time is chosen to be at the time at which the heat flux is at its maximum, thus the time dependent heat flux is

$$q''(t) = q_0'' e^{-\ln 2 \frac{t^2}{\tau_p^2}} \tag{106}$$

where $2\tau_p$ is the full laser pulse width at half of the maximum flux (FWHM), as opposed to the $2t_p$ that was used in Chapter 2, the full width of the laser pulse at $\frac{1}{e}q_0''$.

The laser-powder grain interaction begins with the powder grain absorbing a significant amount of heat from the laser radiation. The surface heat flux will reach its maximum at the time $t = 0$, after which the heat flux will begin to decrease. During the process, the cool sphere interior acts as a heat sink by attempting to thermalize the temperature gradient that is building up within the powder sphere. After the heat flux decreases to a negligible level, several pulse widths after the maximum flux occurs, the

grain finally thermalizes to a uniform temperature throughout the particle. This uniform temperature is reached well before the next laser pulse occurs, and therefore the heat transfer process can be modeled as a recurrence of laser pulses, each of which raise the temperature of the spheres. Essentially, the thermalized temperature of the powder particle from the previous pulse is the initial temperature of the particle when the next pulse begins. In an actual SLS process, melting, and thus consolidation, of the powder bed would occur when the surface temperature of the sphere reaches the melting point of the material, driving the interstitial gasses from the powder bed. This analysis, however, focuses only on the early time of the laser-powder particle interaction in order to find out what will happen before the surface of the powder reaches the melting point.

This paper presents analysis of a one-dimensional model in spherical coordinates of the heat transfer undergone by a single particle in a powder bed subjected to laser heat flux. Another single-particle analysis can be found in Fischer et al. [13]. It is assumed that the liquid phase is incompressible and the melting point of the metal powder is not affected by changes in pressure. The radiation and convection from the surface of the particle are neglected, meaning that the excess heat built up on the surface of the particle must be dissipated in the form of conduction into the powder grain. The simulations will stop when the surface temperature of the powder particle reaches the melting point of the powder. This work forms a basis upon which melting and resolidification of the powder grain may be investigated.

3.1.1 Governing equations

The heat transfer within the powder grain can be described as a pure conduction problem. The heat conduction equation within the grain is

$$\frac{\partial \theta}{\partial t} = \frac{\alpha}{(r_0 - x)^2} \frac{\partial}{\partial x}\left((r_0 - x)^2 \frac{\partial \theta}{\partial x} \right), \quad 0 \le x \le r_0 \tag{107}$$

which is subject to the following initial and boundary conditions

$$\theta \to 0, \quad x \to r_0, \quad t > -\infty \tag{108}$$

$$\theta = 0, \quad 0 \le x \le r_0, \quad t \to -\infty \tag{109}$$

$$\frac{\partial \theta}{\partial x} = 0, \quad x = r_0 \tag{110}$$

The heat flux at the surface is governed by

$$-k_s \frac{\partial \theta}{\partial x} = q''(t), \quad x = 0, \quad t > -\infty \tag{111}$$

where $q''(t)$ is given by Eq. (106).

3.2 The Integral Approximate Solution

When the surface of the powder bed is exposed to heat flux the heat will penetrate the surface and begin to conduct downward. The depth to which the heat flux has penetrated is called the thermal penetration depth, δ, beyond which the temperature is equal to the initial powder bed temperature. Therefore, the following two boundary conditions are valid

$$\theta(x,t) = 0, \quad x \ge \delta(t), \quad t > -\infty \tag{112}$$

$$\frac{\partial \theta}{\partial x} = 0, \quad x \ge \delta(t), \quad t > -\infty . \tag{113}$$

As the heat flux penetrates the surface of the particle the thermal penetration depth, δ, will increase. Since the powder particle has a finite radius, it is certain that at some point during the simulation the thermal penetration depth will reach the center of the particle. For this reason two separate solutions will be needed, one solution for $\delta < r_0$ and one for $\delta = r_0$, both of which are included below.

3.2.1 Solution for $\delta < r_0$

Integrating both sides of Eq. (107) with respect to x in the interval of $(0, \delta)$ yields

$$\int_0^{\delta} (r_0 - x)^2 \frac{\partial \theta}{\partial t} dx = \alpha_s \left[(r_0 - x)^2 \frac{\partial \theta}{\partial x} \right]_0^{\delta} \tag{114}$$

Using Leibniz's rule on the left hand side of Eq. (114) gives

$$\frac{\partial}{\partial t} \int_0^{\delta} (r_0 - x)^2 \theta(x,t) dx - \theta(\delta,t)(r_0 - \delta)^2 \frac{\partial \delta}{\partial t} = \alpha_s \left[(r_0 - x)^2 \frac{\partial \theta}{\partial x} \right]_0^{\delta} \tag{115}$$

Substituting Eqs. (111), (112), and (113) into Eq. (115), the integral energy equation becomes

$$\frac{\partial}{\partial t} \int_0^{\delta} (r_0 - x)^2 \theta(x,t) dx = \frac{\alpha_s q_0'' r_0^2}{k_s} e^{-\ln 2 \frac{t^2}{\tau_p^2}} \tag{116}$$

Assuming that the temperature distribution is a second degree polynomial function of the form

$$\theta(x,t) = A + B(x - \delta) + C(x - \delta)^2 \tag{117}$$

and solving the unknown constants using the boundary conditions of Eqs. (111), (112), and (113), the temperature distribution in the heat affected zone becomes

$$\theta(x,t) = \frac{q_0^{"}(\delta - x)^2}{2k_s\delta} e^{-\ln 2\frac{t^2}{\tau_p^2}}, \quad \delta < r_0 \tag{118}$$

Substituting Eq. (118) into Eq. (116) yields

$$\frac{\partial}{\partial t}\left[\frac{1}{6}\delta^2 e^{-\ln 2\frac{t^2}{\tau_p^2}}\left(r_0^2 - \frac{1}{2}r_0\delta + \frac{1}{10}\delta^2\right)\right] = \alpha_s r_0^2 e^{-\ln 2\frac{t^2}{\tau_p^2}} \tag{119}$$

which is subject to the initial condition

$$\delta = 0, \quad t = -\infty \tag{120}$$

Integrating Eq. (119) with respect to t in the interval $(-\infty, t)$ one obtains

$$\begin{aligned} 0 = \frac{1}{60}\delta^4 e^{-\ln 2\frac{t^2}{\tau_p^2}} - \frac{1}{12}\delta^3 r_0 e^{-\ln 2\frac{t^2}{\tau_p^2}} + \frac{1}{6}\delta^2 r_0^2 e^{-\ln 2\frac{t^2}{\tau_p^2}} \\ - \frac{\alpha_s r_0^2 \tau_p \sqrt{\pi}}{2\sqrt{\ln 2}}\left[1 + erf\left(\sqrt{\ln 2}\,\frac{t}{\tau_p}\right)\right], \quad \delta < r_0, \quad t < t_m \end{aligned} \tag{121}$$

Only one of the roots of Eq. (121) will be both real and positive and this root will be the value of δ for the particular time. Eqs. (118) and (121) sufficiently describe the powder particle when $\delta < r_0$. During the simulation it will be necessary to monitor the value of δ so that we may switch to the alternate solution when necessary. It will also be necessary to monitor the temperature at the surface of the powder particle, $\theta(x = 0, t)$, so that we know when melting begins and the simulation ends.

3.2.2 Solution for $\delta = r_0$

When δ reaches the center of the powder particle the boundary conditions of Eqs. (112) and (113) will no longer be useful. At this point in the preheating stage it will be necessary to assume a temperature profile of a form similar to that of Dombrovski [18]

$$\theta(x,t) = T_c(t)\frac{2r_0 x - x^2}{r_0^2} + \frac{(r_0 - x)^2}{r_0^2} T_{surf}(t) - T_i \tag{122}$$

where $T_c(t)$ is the temperature at the center of the sphere and $T_{surf}(t)$ is the temperature at the surface of the sphere. By examining Eq. (122) it can be seen that the boundary condition of Eq. (110) is already satisfied. Using the boundary condition of Eq. (111) to relate $T_c(t)$ and $T_{surf}(t)$ simplifies Eq. (122) to

$$\theta(x,t) = \frac{q_0^{"}(r_0 - x)^2}{2k_s r_0} e^{-\ln 2\frac{t^2}{\tau_p^2}} + T_c(t) - T_i, \qquad \delta = r_0 \tag{123}$$

This is the assumed temperature profile that will be used for the rest of the integral approximate solution. The only unknown quantity in Eq. (123) is $T_c(t)$ so it is now necessary to find another equation with which to eliminate this parameter. If one proceeds with the integral approximate solution of the as normal this equation will present itself.

Integrating both sides of Eq. (107) with respect to x in the interval of $(0, r_0)$ and applying Leibniz's Rule yields

$$\frac{\partial}{\partial t}\int_0^{r_0} (r_0 - x)^2 \theta(x,t)dx = \alpha_s \left[(r_0 - x)^2 \frac{\partial \Theta}{\partial x} \right]\Bigg|_0^{r_0} \tag{124}$$

Substituting Eq. (111) into Eq. (124), the integral energy equation becomes

$$\frac{\partial}{\partial t}\int_0^{r_0} (r_0 - x)^2 \theta(x,t)dx = \frac{\alpha_s q_0^{"} r_0^2}{k_s} e^{-\ln 2\frac{t^2}{\tau_p^2}} \tag{125}$$

Substituting Eq. (123) into Eq. (125) yields

$$\frac{\partial}{\partial t}\left[\frac{q_0^{"} r_0^4}{10k_s} e^{-\ln 2\frac{t^2}{\tau_p^2}} + \frac{1}{3} r_0^3 \left(T_c(t) - T_i \right) \right] = \frac{\alpha_s q_0^{"} r_0^2}{k_s} e^{-\ln 2\frac{t^2}{\tau_p^2}} \tag{126}$$

which is subject to the initial condition

$$T_c(t) = T_i, \qquad t = t_\delta \tag{127}$$

where t_δ is the time at which δ reaches r_0, the center of the particle. Eq. (126) can be integrated with respect to t in the interval (t_δ, t) to yield

$$\begin{aligned} &\frac{q_0'' r_0^4}{10 k_s}\left[e^{-\ln 2 \frac{t^2}{\tau_p^2}} - e^{-\ln 2 \frac{t_\delta^2}{\tau_p^2}} \right] + \frac{1}{3} r_0^3 \left(T_c(t) - T_i \right) = \\ &\qquad \frac{q_0'' \alpha_s r_0^2 \tau_p \sqrt{\pi}}{2 k_s \sqrt{\ln 2}} \left[erf\left(\sqrt{\ln 2}\, \frac{t}{\tau_p} \right) - erf\left(\sqrt{\ln 2}\, \frac{t_\delta}{\tau_p} \right) \right], \qquad \delta = r_0 \end{aligned} \tag{128}$$

Equation (128) can be rearranged to solve for $\left(T_c(t) - T_i\right)$ which can then be substituted into Eq. (123) to find

$$\begin{aligned} \theta(x,t) = &\frac{q_0''(r_0 - x)^2}{2 k_s r_0} e^{-\ln 2 \frac{t^2}{\tau_p^2}} - \frac{3 q_0'' r_0}{10 k_s}\left[e^{-\ln 2 \frac{t^2}{\tau_p^2}} - e^{-\ln 2 \frac{t_\delta^2}{\tau_p^2}} \right] \\ &+ \frac{3 q_0'' \alpha_s \tau_p \sqrt{\pi}}{2 k_s r_0 \sqrt{\ln 2}} \left[erf\left(\sqrt{\ln 2}\, \frac{t}{\tau_p} \right) - erf\left(\sqrt{\ln 2}\, \frac{t_\delta}{\tau_p} \right) \right], \qquad \delta = r_0, \qquad t < t_m \end{aligned} \tag{129}$$

the equation that describes the temperature profile in the particle after $\delta = r_0$. As with the previous solution, it will be necessary to monitor the temperature at the surface of the powder particle, $\theta(x = 0, t)$, during the simulation so that we know when the melting stage begins. Now that all the necessary components to describe the powder particle have been found a computer simulation can be developed to give the results of the model.

3.3 Results and discussion

After solving the heat transfer problem in terms of various system parameters it was necessary to adapt this solution to use the parameters that describe common laser apparatuses. This was done with the help of Fischer et al. [13]. From this paper the energy in one laser pulse is calculated with the equation

$$E_{pulse} = \frac{1-R}{No} \cdot \frac{P_{av}}{f_{rep}} \left(1 - \frac{1}{e}\right) \tag{130}$$

where R is the reflectivity of the powder grain, P_{av} is the average laser power, f_{rep} is the repetition rate of the laser, and No is the number of powder grains within the optically penetrated disk of powder bed.

$$No = \frac{\frac{\pi}{4} d_p^2 \cdot OPD}{\frac{4}{3} \pi r_0^3} \cdot \frac{\rho_{powder}}{\rho_{bulk}} \tag{131}$$

Equation (131) gives the number of spheres within the disk of powder bed that is optically penetrated, d_p being the diameter of the laser spot and OPD being the optical penetration depth. Combining Eqs. (130) and (131) yields

$$E_{pulse} = \frac{(1-R)\,2(2r_0)^3 \rho_{bulk} P_{av}}{3 d_p^2 OPD \rho_{powder} f_{rep}} \left(1 - \frac{1}{e}\right) \tag{132}$$

the portion of the pulse energy that each particle in the affected region receives based on the previous assumption that multiple scattering leads to a homogenous distribution of energy within the optically penetrated region. Now it is necessary to relate the factor $q_0^{''}$, which is used in the boundary equations for this problem, to the pulse energy received by

the particles. Recognizing that the total energy input to the powder particle by the laser pulse is

$$E_{in} = \int_{-\infty}^{\infty} q_0^{"} e^{-\ln 2 \frac{t^2}{\tau_p^2}} \pi (2r_0)^2 \, dt \tag{133}$$

$$E_{in} = q_0^{"} \pi (2r_0)^2 \frac{\sqrt{\pi}\tau_p}{\sqrt{\ln 2}} \tag{134}$$

and realizing that Eq. (132) must be equal to Eq. (133) gives the final relation of $q_0^{"}$ and the process parameters

$$q_0^{"} = \frac{(1-R)2(2r_0)\rho_{bulk} P_{av} \sqrt{\ln 2}}{3 d_{pulse}^2 OPD \rho_{powder} f_{rep} \pi \sqrt{\pi} \tau_p} \left(1 - \frac{1}{e}\right) \tag{135}$$

Now that the heat transfer problem has been solved for in terms of various system parameters, and these system parameters have been related to real-life laser operating parameters, a computer code was written to simulate the results of the model. The system parameters were then varied to investigate the impact they would have on the process. In all of the following simulations the material properties are that of titanium. The baseline parameters used in the simulation were the experimental values found by Fischer et al. [13], which can be found in the captions of the following figures. The most important processing parameter is clearly the maximum heat flux of the laser pulse, which is proportional to many of the necessary system parameters [see Eq. (135)].

The effect of the superposition of many laser pulses can be seen in Fig. 3.3.1. Initially the powder particle is at room temperature. When the laser pulse heats the particle, the surface temperature rises rapidly and then begins to fall as the heat flux decreases. The temperature rise per pulse is uniform, with the temperature rising about 125 K per pulse. During the ninth pulse the surface temperature of the particle reaches

the melting point of the material, at which point melting begins and the heat transfer simulation is over.

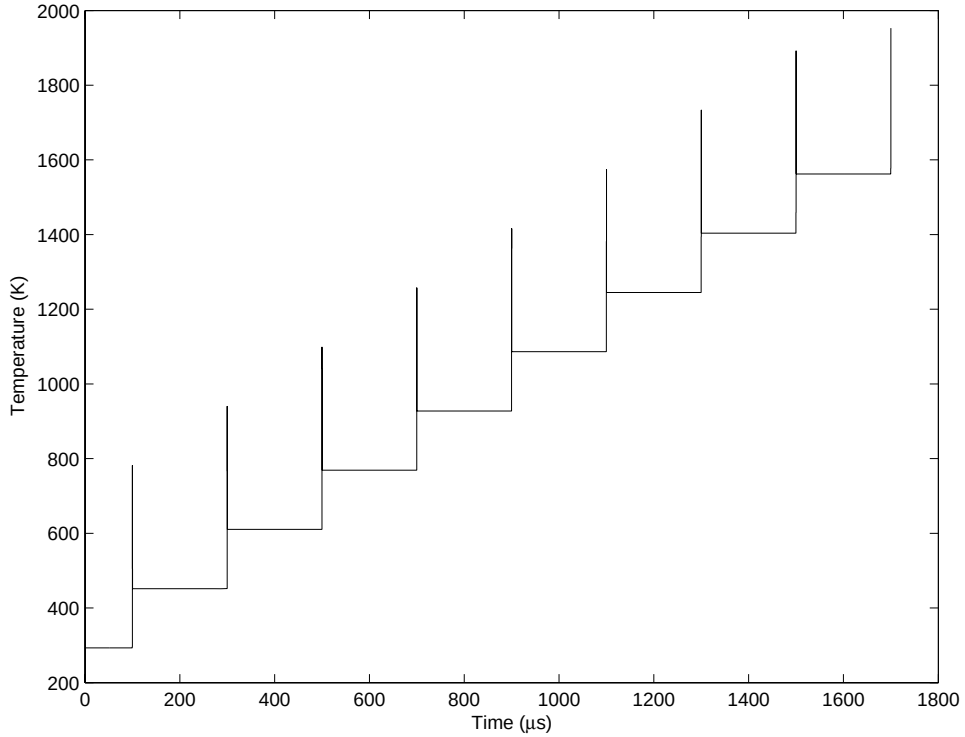

Figure 3.3.1 The effect of multiple laser pulses on a single powder grain.
($r_0 = 11\mu m,\ \tau_p = 75ns,\ f_{rep} = 5kHz,\ T_i = 293K,\ q_0^{"} = 8.587\times10^9 \frac{W}{m^2}$ **)**

Figure 3.3.2 shows the switch from the $\delta < r_0$ solution to the $\delta = r_0$ solution. Previous to the dimensionless time $\tau = 1.7$ the thermal penetration depth increases as the temperature at the surface rises and then begins to fall. When δ reaches the center of the particle the secondary solution begins, and we see the core temperature of the particle, the lower curve, begin to rise. As the heat flux continues to decrease the two curves meet, at which point the powder particle has thermalized to a uniform temperature. The style of

the upper plot of Fig. 3.3.2 will be the preferred visualization method for evaluating the effects of a change in a particular system parameter.

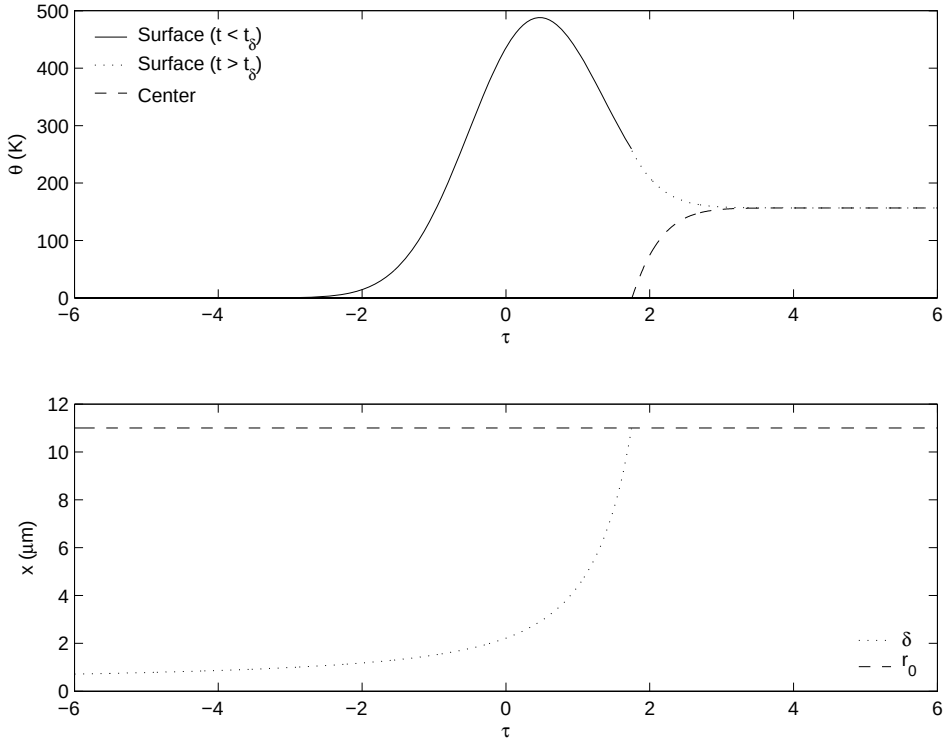

Figure 3.3.2 The excess temperature at the surface and core of the sphere in time and the corresponding thermal penetration depth.

($r_0 = 11\mu m,\ \tau_p = 75ns,\ f_{rep} = 5kHz,\ q_0^{"} = 8.587\times10^9 \frac{W}{m^2}$ **)**

Figure 3.3.3 shows the temperature profile within the sphere at various nondimensional times during a simulation for the baseline values of the system parameters. It shows an increase in temperature throughout the powder bed as the process continues. The line corresponding to $\tau = 0.473$ is the time at which the surface of the powder particle reaches its maximum temperature. Note that the temperature

profile lines for $\delta < r_0$ do not initially extend all the way to $x = r_0 = 11\mu m$ but do after the transition to the alternate solution is made at the time $\tau = \tau_\delta$.

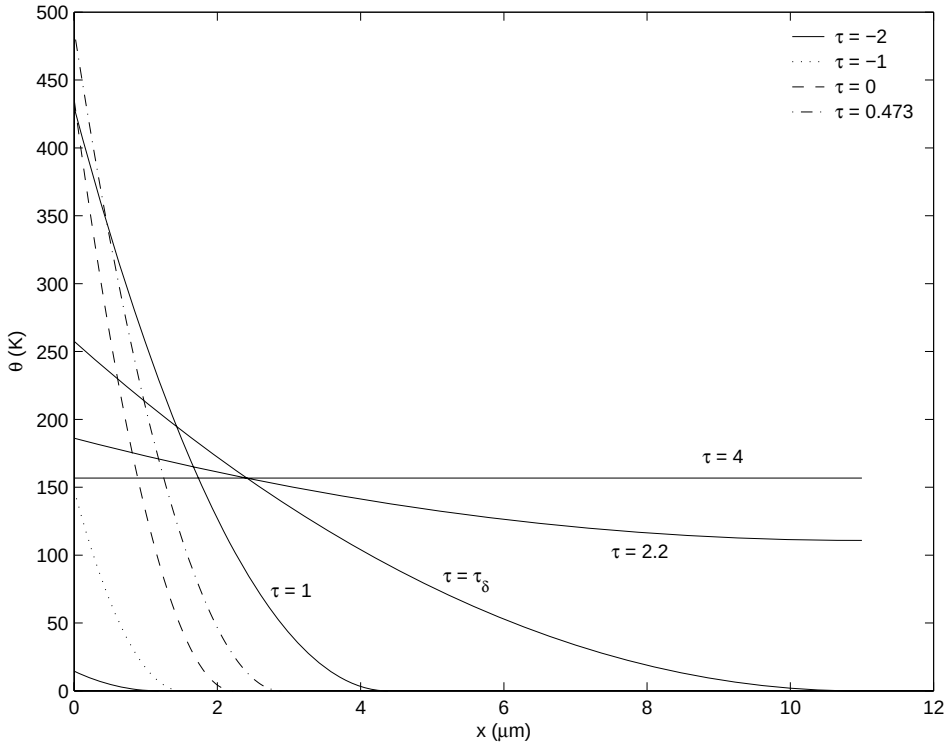

Figure 3.3.3 The temperature profile within the powder particle at various times.
($r_0 = 11\mu m,\ \tau_p = 75ns,\ f_{rep} = 5kHz,\ q_0^{"} = 8.587 \times 10^9 \frac{W}{m^2}$ **)**

Figure 3.3.4 shows the surface temperature of the powder particle for various laser repetition rates. Because the average power of the laser, P_{av}, does not change with time, an adjustment of the repetition rate f_{rep} greatly affects the maximum heat flux delivered to the particle per pulse. A repetition rate of $5kHz$ delivers one large pulse in $200\mu s$, a repetition rate of $15kHz$ delivers three medium sized pulses in $200\mu s$, and a repetition rate of $25kHz$ delivers five small pulses in $200\mu s$. Since the total energy deposited

during the $200\mu s$ is the same, the final temperature of the particle at the end of a particular period is the same for all repetition rates. This behavior could be used to limit the temperature rise per pulse to a desired value, or perhaps vice versa.

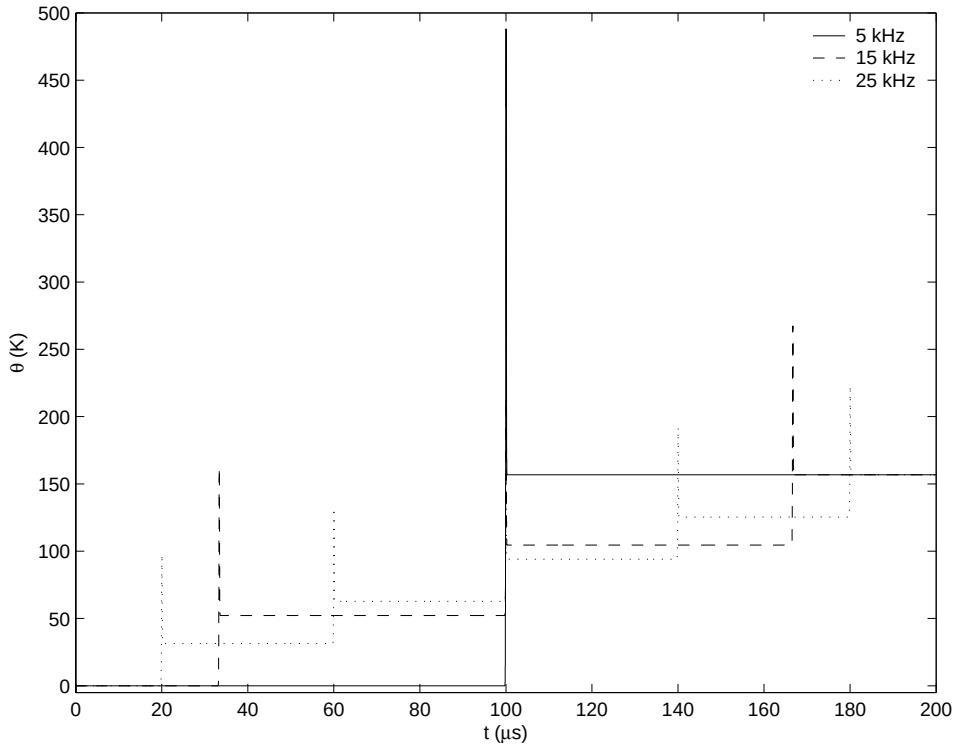

Figure 3.3.4 The surface temperature of the sphere with respect to time for various laser pulse repetition rates. ($r_0 = 11\mu m,\ \tau_p = 75ns$)

Figure 3.3.5 demonstrates the same behavior as Fig. 3.3.4 on a smaller time scale. As expected, the one large pulse raises the temperature of the powder grain surface quite a bit more than the smaller pulses, but the time at which surface temperature begins to rise is unaffected. The time at which δ reaches r_0 is also unchanged. This is because the

time necessary to penetrate the particle depends only on r_0, τ_p, and α_s, which can be seen by examining Eq. (121).

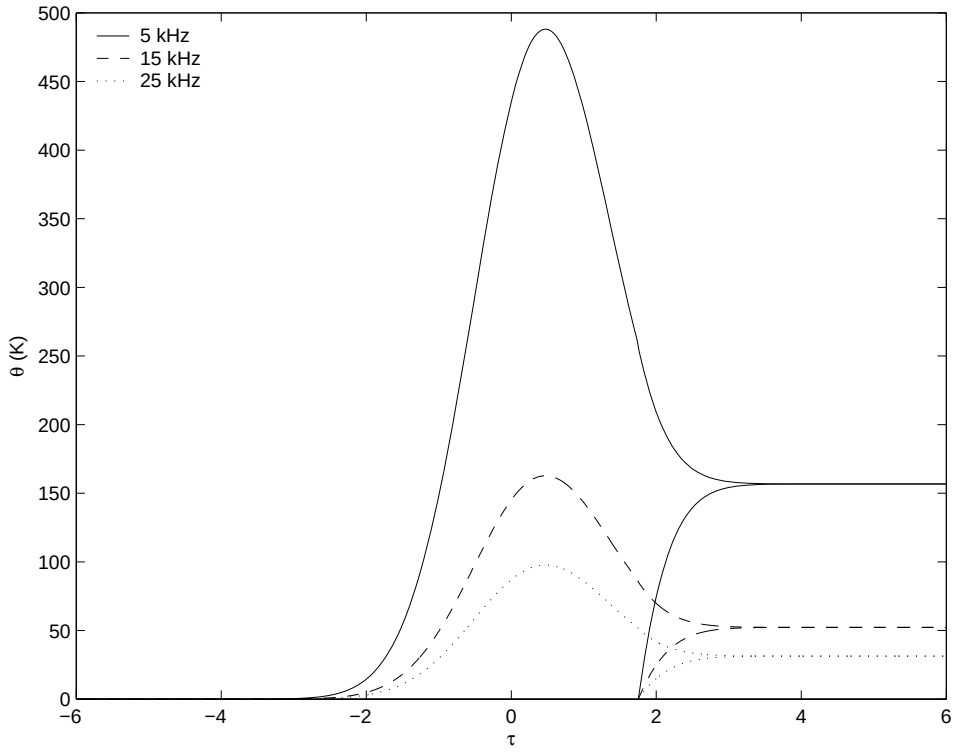

Figure 3.3.5 The surface and center temperature of the sphere for different pulse repetition rates. ($r_0 = 11\mu m,\ \tau_p = 75ns$)

Figure 3.3.6 demonstrates the effect of the maximum heat flux on the heat transfer in the powder particle. As was seen with a change in the repetition rate of the laser, an increase in maximum heat flux will result in a higher temperature rise on the surface of the particle, as well as a higher thermalized particle temperature after the laser pulse is finished. The time at which the surface temperature begins to rise and the time at which

the particle is fully penetrated will not change when the surface heat flux varies, as mentioned previously.

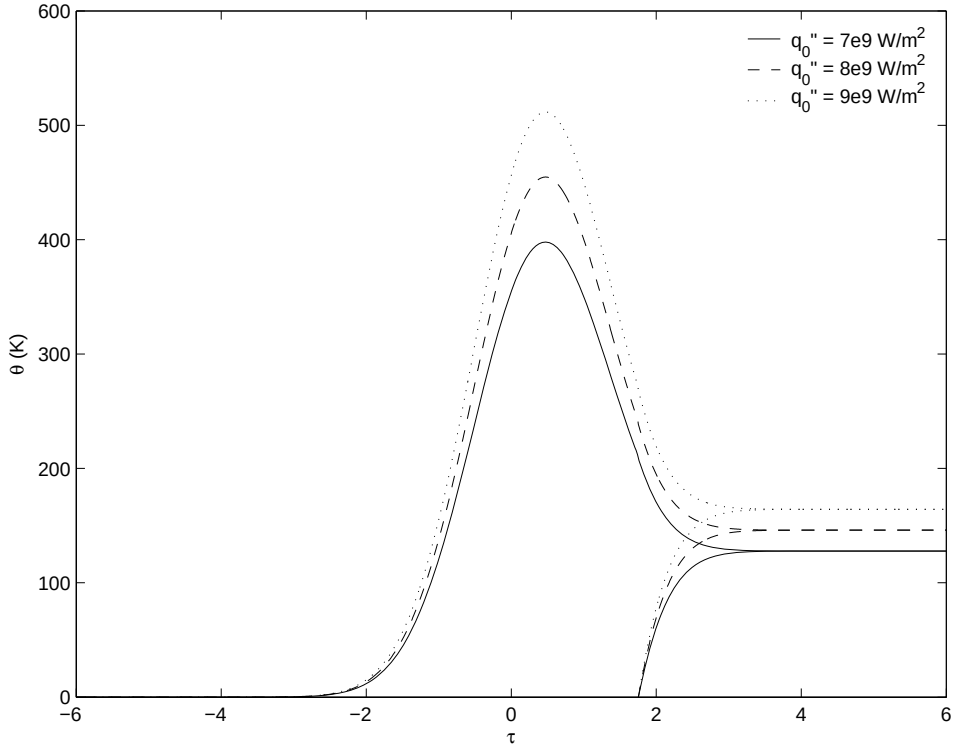

Figure 3.3.6 The surface and core temperatures within the sphere for different values of maximum heat flux. ($r_0 = 11\mu m,\ \tau_p = 75ns$ **)**

The effects of a change in the width of the laser pulse, τ_p, are shown in Fig. 3.3.7. Since the energy per pulse is constant, even for a change in τ_p, a wider pulse will essentially deliver its energy over a longer time period than that of a smaller pulse. Since the energy per pulse is unchanged, the temperature rise per pulse will also be unchanged. Although the energy per pulse is unchanged, the magnitude of q_0'' must decrease for an

increase in τ_p [see Eq. (134)], which explains difference in peak temperatures displayed in Fig. 3.3.7. Because of the presence of τ_p in Eq. (121), τ_δ decreases when τ_p increases.

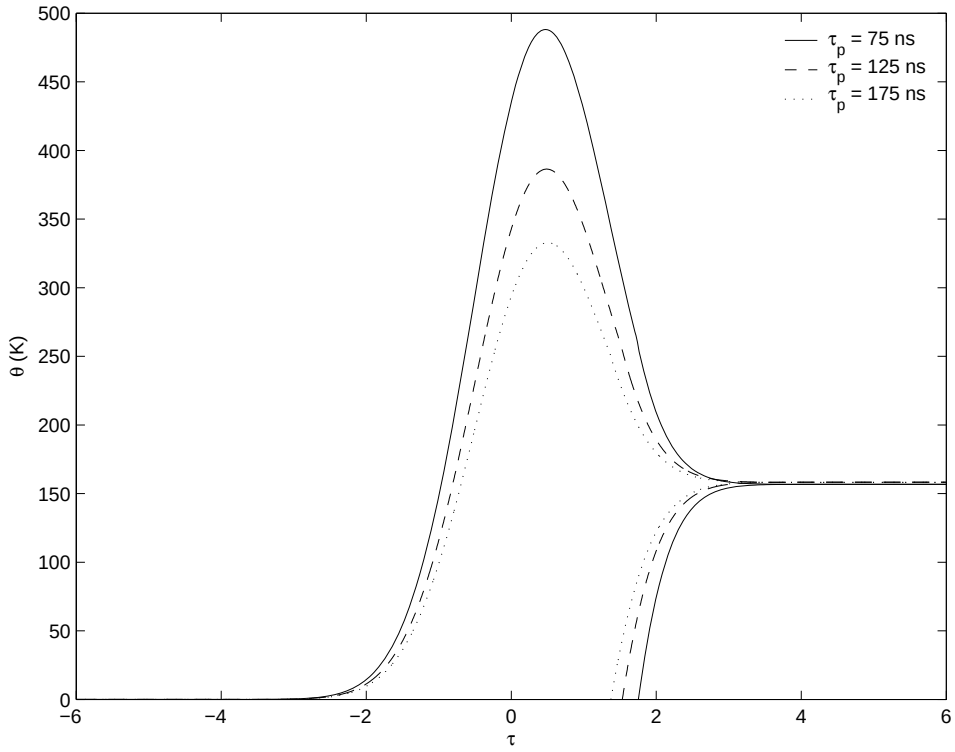

Figure 3.3.7 The surface and core temperature of the powder particle for different pulse widths of the laser heating source. ($r_0 = 11\mu m,\ f_{rep} = 5kHz$ **)**

In Fig. 3.3.8 one can see that when the radius of the powder particle decreases the time necessary for the heat flux to penetrate to the center of that particle noticeably decreases. This makes perfect sense because a sphere that is very small will clearly take less time to heat than a sphere that is very large. Figure 3.3.8 shows that as the radius of the heated sphere decreases the peak temperature at the surface of that sphere also

decreases. This makes sense when considering that many more small spheres can fit into a particular volume than larger spheres. If there are more spheres in one volume than in another, and both volumes are exposed to the same amount of laser heating, then the smaller spheres will have less energy per particle and therefore will be heated to a lesser degree. Although a discrepancy exists where peak temperatures are concerned, the thermalized temperatures of the spheres are all the same. This is because the larger

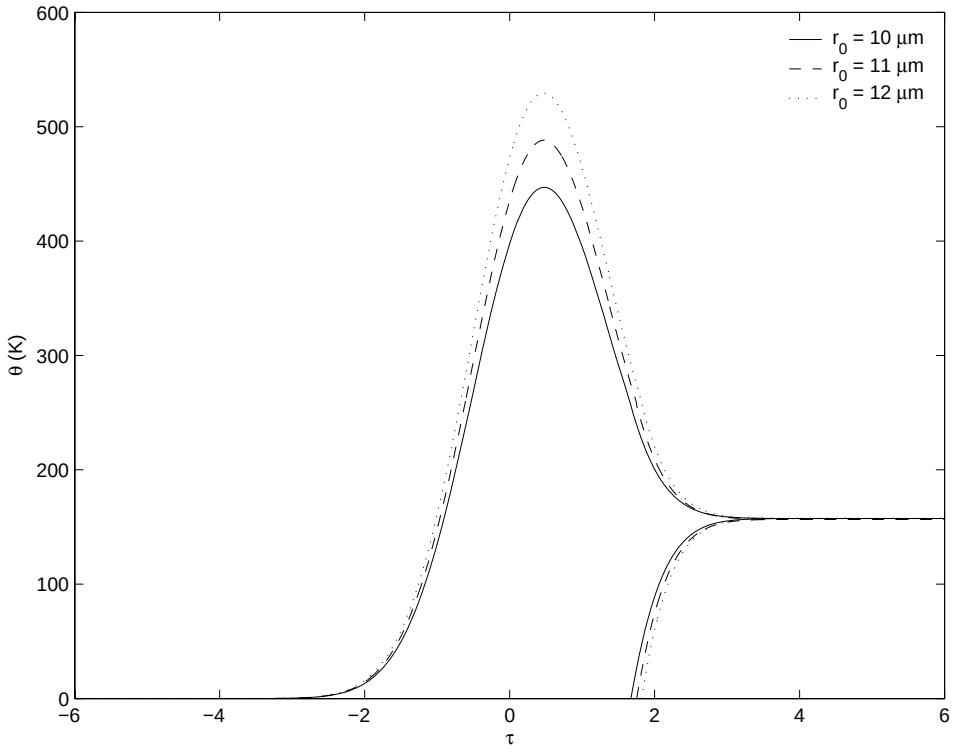

Figure 3.3.8 The effect of a change in particle radius on surface and core temperature of the powder grain. ($\tau_p = 75ns,\ f_{rep} = 5kHz$ **)**

sphere gets hotter on the surface but has more inner material to heat. The smaller sphere on the other hand does not get as hot on the surface, but heats its smaller interior to the same temperature as that of the larger sphere. One can also see from the plot that a smaller sphere will thermalize faster than a larger sphere, which also makes sense.

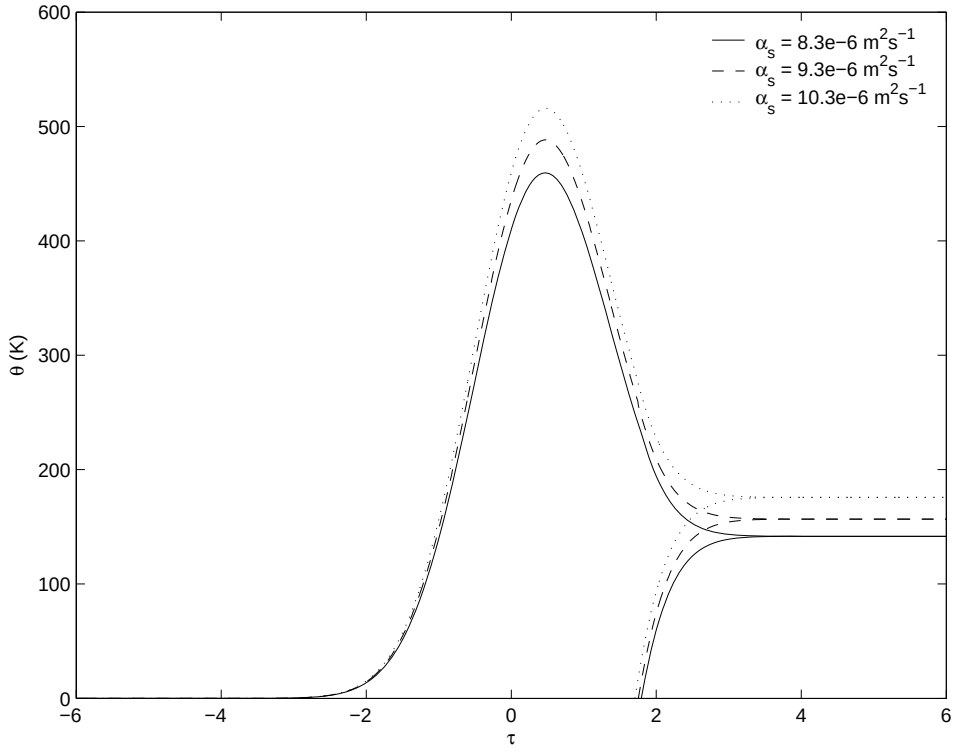

Figure 3.3.9 The effect of a change in thermal diffusivity on surface and core temperature of the powder grain. ($r_0 = 11\mu m,\ \tau_p = 75ns,\ f_{rep} = 5kHz$ **)**

Figure 3.3.9 shows the effect of a change in thermal diffusivity of the heated material. Thermal diffusivity is a function of the specific heat, density, and thermal conductivity of a material, so a change in thermal diffusivity represents a change in any of these properties. In this particular simulation, all three of these properties are constants,

however it is still interesting to see how a change in thermal conductivity affects the temperature curves. An increase in the thermal diffusivity results in a higher peak temperature at the surface of the sphere. Since the input energy is the same for all three pulses, this effect could be caused by a decrease in specific heat of the metal, which would mean that less energy is needed to raise the temperature of the sphere, producing both the higher peak temperature and the higher thermalized temperature seen in Fig. 3.3.9. The figure also shows that the time necessary for the heat flux to completely penetrate the sphere does decrease with an increase in thermal diffusivity.

3.4 Conclusion

Heat transfer in a single powder particle subjected to nanosecond pulsed laser heating was investigated analytically. The only process parameter that did not have an effect on the heating of the particle was the initial temperature. This is because the change in temperature of the particle increases the same amount with each pulse, regardless of its previous temperature. When the effects of many laser pulses are superpositioned upon each other the particle can be rapidly heated to its melting point, at which time the simulation is over.

A change in the repetition rate of the laser affects mainly the maximum heat flux delivered to the particle per pulse. An increase in maximum heat flux will result in a higher temperature rise on the surface of the particle, as well as a higher thermalized particle temperature after the laser pulse is finished. The time at which the particle is fully penetrated will not change when the surface heat flux varies. A change in the width of the laser pulse, τ_p, will not affect the thermalized temperature, however, τ_δ will decrease when τ_p increases. When the radius of the powder particle decreases the time

necessary for the heat flux to penetrate to the center of that particle will also decrease. A decrease in the radius of the sphere results in a decrease of the peak temperature at the surface of the sphere. Although a discrepancy exists where peak temperatures are concerned, the thermalized temperatures of different-sized spheres are all the same. An increase in the thermal diffusivity of the material results in a higher peak temperature at the surface of the sphere as well as a higher thermalized temperature. The time necessary for the heat flux to completely penetrate the sphere does decrease with an increase in thermal diffusivity.

Chapter 4. Summary, conclusions, and future work

4.1 Summary and conclusion

Melting and resolidification of a one-dimensional, subcooled powder bed with infinite thickness subjected to temporal Gaussian heat flux was investigated analytically. The integral approximate solution was used to obtain solutions for preheating, melting with shrinkage, and resolidification. An efficient computer code was then written to simulate the process and the effects of the system parameters were investigated. It is clear that all process parameters have effects on the results of the SLS process but through nondimensionalization the number of independent parameters was significantly reduced.

It was found that the Stefan number was the most important parameter in the simulation. As the Stefan number increases the melt pool depth and melt pool surface

temperature also increase. Due to the relatively large liquid pool the overall process time is increased significantly. This is because the only way for the liquid pool to resolidify is by dissipating its heat into the powder bed, as heat loss from the surface is neglected. As subcooling of the powder bed increases more heat flux is needed to melt the powder, and thus the melt pool is shallower. It was found that a very porous powder bed will reach the end of the preheating period faster than a less porous one because the interstitial gas greatly decreases the thermal conductivity of the powder bed. Because more heat is kept at the surface of the powder bed a greater amount of material will be sintered, therefore increasing the total process time. An increase in the fraction of low-melting-point powder will mainly increase the process time because a large amount of liquid takes a long time to solidify.

Heat transfer in a single powder particle subjected to nanosecond pulsed laser heating was also investigated analytically. Because of symmetry the particle was considered to be one-dimensional. The integral approximate solution was used to obtain the location of the thermal penetration depth. Since the particle under consideration was of finite thickness, it was necessary to obtain two time-dependent solutions, one for $\delta < r_0$ and one for $\delta = r_0$. A computer code was then written to simulate the results of the analysis and the process parameters varied to investigate their effects on the heat transfer within the powder sphere. The only process parameter that did not have an effect on the heating of the particle was the initial temperature. This is because the change in temperature rise of the particle is uniform for every pulse, regardless of its previous temperature. If many laser pulses are simulated one after another then the particle can be rapidly heated to its melting point, at which time the heat transfer simulation is over.

As in the previous investigation, the heat flux input to the surface of the sphere was found to be the most important parameter. A change in the repetition rate of the laser affects mainly the maximum heat flux delivered to the particle per pulse. Since the average power of the laser does not change, an adjustment of the pulse frequency is the easiest way to change the maximum flux provided by the laser. An increase in maximum heat flux will clearly result in a higher temperature rise on the surface of the particle, as well as a higher thermalized particle temperature after the laser pulse is finished. The time at which the particle is fully penetrated does not change as the surface heat flux varies. Only a change in r_0, τ_p, or α_s will change when the thermal penetration depth reaches the center of the powder grain. A decrease in the radius of the sphere in question results in a decrease of the peak temperature at the surface of the sphere. Although a discrepancy exists where peak temperatures are concerned, the thermalized temperatures of different-sized spheres are all the same. When the radius of the powder particle decreases the time necessary for the heat flux to penetrate to the center of that particle will also decrease. A change in the width of the laser pulse, τ_p, will not affect the thermalized temperature, however, τ_δ will decrease when τ_p increases. An increase in the thermal diffusivity of the material results in a higher peak temperature at the surface of the sphere as well as a higher thermalized temperature. The time necessary for the heat flux to completely penetrate the sphere does decrease with an increase in thermal diffusivity. The physical model and results of this investigation pave the way for further modeling of SLS processes with a pulsed laser.

4.2 Future work

Since many SLS processes rely on empirical data the need for an accurate model is very real. Although the previous work does provide insight into the important parameters of the SLS process there are still many more opportunities for continued research. Modeling of the particle-level interaction between a metal powder grain and a nanosecond laser could be continued. The logical next step to the model presented in Chapter 3 is to analyze the melting and resolidification of the liquid skin on the surface of the individual powder grains. The integral approximate solution could be used in a fashion similar to that of Chapter 2 to solve this problem. With a model of this nature, the degree of partial melting in the powder bed could be easily predicted, and thus controlled, ultimately allowing for control of the local porosity in the final product. Such a model could have applications not only in SLS research, but perhaps other melting and freezing applications, such as mushy-zone problems.

The effect of vaporization of the metal powder particles on the powder bed is also a topic which requires looking into. A certain amount of recoil pressure created by vaporization at the surface of the powder bed could serve to prevent the balling effect by disrupting the surface tension of the balls as they occur. Too much recoil pressure, however, could blow the powder away before any consolidation can take place.

Another possible opportunity for research is the integration of the two scales of SLS modeling presented above. A particle level model contained within a powder bed level model could be a very powerful tool in the development of improved SLS techniques. The above work provides direction to those interested in doing research and experiments

in the SLS field. In time a powerful heat transfer model will be developed so that the precision and quality of SLS processes can be accurately and quickly predicted.

REFERENCES

[1] M. Agarwala, D. Bourell, J. Beaman, H. Marcus, J. Barlow, Direct selective laser sintering of metals, Rapid Prototyping Journal, 1 (1) (1995) 26 – 36.

[2] S. Das, J. Beaman, M. Wohlert, D. Bourell, Direct laser freeform fabrication of high performance metal components, Rapid Prototyping Journal, 4 (3) (1998) 112 – 117.

[3] P. Fischer, V. Romano, H.P. Weber, N.P. Karapatis, E. Boillat, R. Glardon, Sintering of commercially pure titanium powder with a Nd:YAG laser source, Acta Materialia, 51 (6) (2003) 1651 – 1662.

[4] F. Abe, E. Costa Santos, Y. Kitamura, K. Osakada, M. Shiomi, Influence of forming conditions on the titanium model in rapid prototyping with the selective laser melting process, Proceedings of the Institution of Mechanical Engineers Part C – Journal of Mechanical Engineering Science, 217 (1) (2003) 119 – 126.

[5] N.K. Tolochko, S.E. Mozzharov, I.A. Yadroitsev, T. Laoui, L. Froyen, V.I. Titov, M.B. Ignatiev, Balling processes during selective laser treatment of powders, Rapid Prototyping Journal, 10 (2) (2004) 78 – 87.

[6] D.E. Bunnell, Fundamentals of selective laser sintering of metals, PhD thesis, University of Texas at Austin, Austin, TX, 1995.

[7] T. Manzur, T. DeMaria, W. Chen, C. Roychoudhuri, Potential role of high power laser diode in manufacturing, SPIE Photonics West Conference, San Jose, CA, 1996.

[8] C. Konrad, Y. Zhang, B. Xiao, Analysis of melting and resolidification in a two-component metal powder bed subjected to temporal Gaussian heat flux, International Journal of Heat and Mass Transfer, (2005) Article in Press.

[9] Y. Zhang, A. Faghri, Melting of a subcooled mixed powder bed with constant heat flux heating, International Journal of Heat and Mass Transfer, 42 (5) (1999) 775 – 788.

[10] T. Chen, Y. Zhang, Analysis of melting in a mixed powder bed with finite thickness subjected to constant heat flux heating, Proceeding of ASME Summer Heat Transfer Conference, Las Vegas, NV, July 21-23, 2003.

[11] R. Morgan, C.J. Sutcliffe, W. O'Neill, Experimental investigation of nanosecond pulsed Nd:YAG laser re-melted pre-placed powder beds, Rapid Prototyping Journal, 7 (3) (2001) 159 – 172.

[12] P. Fischer, V. Romano, H.P. Weber, S. Kolossov, Pulsed laser sintering of metallic powders, Thin Solid Films, 453-454 (2004) 139 – 144.

[13] P. Fischer, N. Karapatis, V. Romano, R. Glardon, H.P. Weber, A model for the interaction of near-infrared laser pulses with metal powders in selective laser sintering, Applied Physics A, 74 (4) (2002) 467 – 474.

[14] R. Viskanta, Phase change heat transfer, in: G.A. Lane (Ed.), Solar heat storage: latent heat materials, CRC Press, Boca Raton, FL, 1983.

[15] L.S. Yao, J. Prusa, Melting and freezing, Advances in Heat Transfer, 19 (1989), 1 – 95.

[16] W-N Su, P. Erasenthiran, P.M. Dickens, Investigation of fully dense laser sintering of tool steel powder using a pulsed Nd: YAG (neodymium-doped yttrium aluminum garnet) laser, Proceedings of the Institution of Mechanical Engineers Part C-Journal of Mechanical Engineering Science, 217 (1) (2003) 127 – 138.

[17] G.R. Hadley, Thermal conductivity of packed metal powders, International Journal of Heat and Mass Transfer, 29 (6) (1986) 909 – 920.

[18] L.A. Dombrovsky, A simplified non-isothermal model for droplet heating and evaporation, International Communications in Heat and Mass Transfer, 30 (6) (2003) 787 – 796.